E. Andreis, V. Franzese, F. Topputo
Onboard Orbit Determination for Deep-Space CubeSats
Journal of Guidance Control and Dynamics, Published online 04/04/2022
doi:10.2514/1.G006294

On-board Orbit Determination for Deep-Space CubeSats

Eleonora Andreis * and Vittorio Franzese †
Politecnico di Milano, 20156, Milan, Italy

Francesco Topputo ‡
Politecnico di Milano, 20156, Milan, Italy

In this work, an orbit determination algorithm suitable for CubeSats onboard implementation is developed, which simulates optical autonomous navigation accomplished by a stand-alone platform. An extended Kalman filter featuring line-of-sight acquisitions of planets is selected as the state estimator, and its performances are tested on a Raspberry Pi, whose characteristics are comparable to a miniaturized onboard computer. An improvement of the solution accuracy is performed by correcting the planetary light-time and aberration effects as well as by exploiting the optimal beacons selection strategy to acquire the external observations. Moreover, the numerical precision of the estimator is improved through the implementation of factorization techniques and non-dimensionalization strategies. The results are presented for a sample Earth–Mars transfer, where the time slot for the navigation campaign involves 2 hours every 10 days. At final time, the probe position and velocity are estimated with a 3σ accuracy of 360 km and 0.04 m/s, respectively.

I. Introduction

A new era of space exploration is fast approaching. CubeSats, shoe-boxed spacecraft, have triggered a revolution in the way satellites have been launched into space, owing to their low cost compared to traditional spacecraft [1]. The exploitation of standardized dimensions and Commercial-Off-The-Shelf (COTS) components have boosted their utilization by reducing the mission cost and development time [2]. Although most of the nanosatellites have been thus far launched into Low Earth Orbits (LEO), a number of CubeSats applications in deep space is foreseen [3].

In 2018, two deep-space CubeSats were deployed by NASA inside the Mars Cube One (MarCO) experiment [4] as part of the Interior Exploration using Seismic Investigations, Geodesy, and Heat Transport (InSight) mission [5]. In November 2021, NASA is expected to launch thirteen 6U-sized CubeSats along

*Ph.D. Candidate, Department of Aerospace Science and Technology, Via La Masa, 34, eleonora.andreis@polimi.it
†Postdoctoral Research Fellow, Department of Aerospace Science and Technology, Via La Masa, 34, vittorio.franzese@polimi.it
‡Full Professor, Department of Aerospace Science and Technology, Via La Masa, 34, francesco.topputo@polimi.it, AIAA Senior Member

with Artemis I mission, which will be operative after the trans-lunar injection burn*. Other innovative nanosats mission concept proposals have been funded by ESA, among them there are the Lunar Meteoroid Impacts Observer (LUMIO) [6, 7], the Miniaturised Asteroid Remote Geophysical Observer (M-ARGO) [3][8], Juventas [9] and Milani [10] as part of Hera mission [11].

The CubeSats impact on the number of interplanetary missions will be tremendous, making it unsustainable to pilot them from the ground. The current paradigm for deep-space navigation relies heavily on radiometric tracking [12]. Radiometric navigation yields sub-meter and sub-centimeter per second accuracy in position and velocity, respectively, but still requires ground stations and human-in-the-loop operations. Ground control introduces critical delays and takes a large share of the space mission cost, so hampering the full mission scalability. Moreover, the standard practice will restrict the number of controllable spacecraft since ground facilities will saturate soon due to the rapid proliferation of deep-space assets [13]. At the current development pace, human-in-the-loop navigation will soon become unsustainable. Miniaturized probes that can perform guidance, navigation, and control operations without human instructions are key.

One of the first flight tests of an onboard autonomous navigation system (AutoNav) was performed within the Deep-Space 1 (DS1) mission in 1998 using optical navigation [14–16]. The idea is to take images of unresolved targets while in deep space, from which the inertial Line-Of-Sight (LoS) vectors are extracted [17]. The LoS vectors are then input into an orbit determination (OD) algorithm, which reconstructs the spacecraft state. In deep space, the onboard electro-optical sensor can extract information by observing unresolved planets, asteroids, or both, depending on the camera performances. For DS1, bright asteroids in the asteroid belt were exploited as beacons. Moreover, the tracked targets were selected on the ground and uploaded to the probe. In [18, 19] it is demonstrated that a correlation exists between the geometrical position of the beacons relative to the probe and the solution accuracy of a static OD algorithm. Besides, the solution of the OD problem in deep space can be enhanced by correcting the error generated in the estimation of the LoS directions caused by the light-time and light aberration effects. For this purpose, these two corrections are implemented in an Extended Kalman Filter (EKF) simultaneously in [20], both downstream of the state propagation. In [21] a strategy to correct for the relativistic effects is proposed, in which the stellar aberration is exploited as navigation observable to estimate the probe velocity. Among CubeSats missions , the aforementioned M-ARGO aims to assess the feasibility of an autonomous navigation algorithm during the interplanetary transfer toward the target asteroid [22]. In this context, the miniaturized NavCam will acquire optical measurements from celestial bodies like planets, which will be processed onboard and fed to an estimator to obtain the probe state [8]. When the deployment of the OD algorithm has to be performed on a CubeSat processor, its numerical robustness and computational complexity have to be assessed. For example, Song [23] solves the deep-space OD problem by applying the UD factorization to the EKF. In this

*`https://www.nasa.gov/artemis-1`, last visited on March 2021

way, the numerical stability and the computational efficiency of the filter are enhanced.

In this work, an autonomous optical-based OD algorithm deployable on a representative CubeSat processor is presented. The estimation technique proposed here is intended for use during the cruise phase of a interplanetary mission toward Mars in the framework of the EXTREMA project [24]. With the algorithm proposed, the position should be estimated with errors on the order of 1000 km during the targeting, which is about one order of magnitude below the orbit determination requirement by the project. .

The contribution to the state-of-art is threefold. First, the solution accuracy of the estimation is improved thanks to the introduction of light effects corrections and to the exploitation of an optimal strategy to select the best planets to observe. Second, the estimator numerical stability and computational performances are enhanced through the implementation of factorization techniques and non-dimensionalization strategies. Third, the navigation algorithm is deployed and tested on a platform comparable to a CubeSat processor as experimental proof of the suitability of the selected OD algorithm. The optimal beacons selection strategy derived in [8] is here applied to an on-board dynamic estimator. The implementation is embedded into the filter by taking as input the estimated probe position instead of a reference trajectory. Moreover, the light-time correction is performed following an innovative procedure: Differently from the one introduced in [20], the epoch at which light is emitted by the beacons is retrieved online by solving a nonlinear equation after the filter propagation steps. The beacons ephemerides can be so retrieved at the time of light emission, instead of the onboard time, so correcting for the light-time effect.

The paper is structured as follows. In Sec. II the methodology is presented. Firstly, the problem geometry is introduced in Sec. II.A, and the corrections of the light-time and light aberration effects are derived in Secs. II.B and II.C. Then, the adoption of the optimal beacons selection strategy for the acquisition of the external observations is shown in Sec. II.D. The EKF is so implemented in Sec. III: Moving from a standard filtering scheme (Sec. III.D), alternative techniques are then implemented in Sec. III.E to solve the numerical issues that can arise after the onboard deployment of the algorithm. In Sec. IV the results of the implementation are illustrated. In particular, the performances of the five filtering approaches are compared in terms of numerical stability and computational complexity in Sec. IV.B. The deployment of the best alternative on a computational board comparable to a CubeSat miniaturized On-Board Computer is eventually performed in Sec. IV.C.

II. Statement of the Problem

A. Problem Geometry

In deep space a spacecraft can estimate its position by acquiring optical information from the observations of unresolved planets. The Line-of-Sight (LoS) to the planets, whose extraction from images is covered in

literature [15, 25] , are used to feed the on-board navigation method, from which the probe state is estimated.

When two LoS directions associated to different planets are acquired simultaneously, the kinematic celestial triangulation problem can be solved [20]. With reference to Fig. 1, let $\boldsymbol{r}$ be the spacecraft position. Then,

$$\boldsymbol{r} = \boldsymbol{r}_1 - \rho_1 \hat{\boldsymbol{\rho}}_1 = \boldsymbol{r}_2 - \rho_2 \hat{\boldsymbol{\rho}}_2 \tag{1}$$

where $\boldsymbol{r}_i$ denotes the position of planet i, ρ_i is the observer range to planet i, and $\hat{\boldsymbol{\rho}}_i$ its direction. Considering the two-planets observation scenario, the ranges ρ_1, ρ_2 are unknown; yet, $\hat{\boldsymbol{\rho}}_1$, $\hat{\boldsymbol{\rho}}_2$ are measured. The scalar multiplication of Eq. (1) by $\hat{\boldsymbol{\rho}}_1$ and $\hat{\boldsymbol{\rho}}_2$ yields to a system of two equations which can be arranged in matrix form as

$$\underbrace{\begin{bmatrix} -1 & \hat{\boldsymbol{\rho}}_1^\top \hat{\boldsymbol{\rho}}_2 \\ -\hat{\boldsymbol{\rho}}_2^\top \hat{\boldsymbol{\rho}}_1 & 1 \end{bmatrix}}_{\boldsymbol{A}} \underbrace{\begin{bmatrix} \rho_1 \\ \rho_2 \end{bmatrix}}_{\boldsymbol{x}} = \underbrace{\begin{bmatrix} \hat{\boldsymbol{\rho}}_1^\top (\boldsymbol{r}_2 - \boldsymbol{r}_1) \\ \hat{\boldsymbol{\rho}}_2^\top (\boldsymbol{r}_2 - \boldsymbol{r}_1) \end{bmatrix}}_{\boldsymbol{b}} \tag{2}$$

described by the linear-algebra problem, $\boldsymbol{A}\boldsymbol{x} = \boldsymbol{b}$. The solution to Eq. (2) exists as long as $\Delta(\boldsymbol{A}) \neq 0$, where Δ is the determinant of $\boldsymbol{A}$. Let γ be the angle between the two planets as seen by the observer (Fig. 1), then $\cos\gamma = \hat{\boldsymbol{\rho}}_1^\top \hat{\boldsymbol{\rho}}_2$ and thus $\Delta(\boldsymbol{A}) = -1 + \cos^2\gamma$. When $\cos\gamma = \pm 1$, $\boldsymbol{A}$ is singular and the solution is undetermined. This occurs when the probe and the planets are in conjunction or opposition [18]. For $\Delta(\boldsymbol{A}) \neq 0$, the solution to the problem is $\boldsymbol{x} = \boldsymbol{A}^{-1}\boldsymbol{b}$, which plugged into Eq. (1) provides the spacecraft inertial position. The method presented so far solves for the spacecraft position at the same epoch of measurements acquisition. Dynamic methods, e.g., Kalman filtering, are however more accurate and can estimate the full state vector, including the spacecraft velocity. Before dealing with the Kalman filter formulation, however, the effects of the light-time correction (Sec. II.B) and celestial aberration (Sec. II.C) are introduced, together with an optimal beacons selection strategy (Sec. II.D).

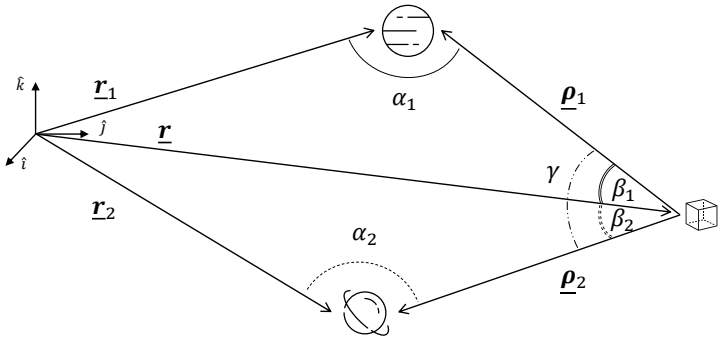

Fig. 1 Celestial triangulation geometry in the Sun-centered frame with characteristic angles; β: Solar Aspect Angle (SAA); α: planet's phase angle; γ: angle between the directions of the two planets as seen by the observer.

Moreover, the following conservative assumptions are made to specialize the problem to the case of interplanetary CubeSats. 1) Only one miniaturized imager (star tracker or navigation camera) is adopted on board. 2) Because of the limited performances of the sensor, minor bodies are not always detected [19], and therefore only the planets are used to get the $\hat{\boldsymbol{\rho}}_i$ measurements. 3) Only one planet at a time is tracked, and a slew maneuver is needed to point to the second beacon; that is, differently from the standard celestial triangulation in [20], planets measurements are acquired asynchronously. 4) Only a pair of planets is observed in each acquisition window; this is to limit the time slot allocated to navigation.

B. Light-time Effect Correction

Due to the finite speed of light and to the enormous distance between the satellite and the beacon, the time difference between the emission and the reception of the luminous signal is significant. The light received by the imager at epoch t has been emitted by the observed planet at a previous epoch τ, thus $\tau < t$. This effect, called light-time, yields to a systematic error when neglected [26].

With reference to Fig. 2, the relative position vector of the beacon is better expressed as

$$\boldsymbol{\rho}(t,\tau) = \boldsymbol{r}_i(\tau) - \boldsymbol{r}(t) \tag{3}$$

where $\boldsymbol{r}_i(\tau)$ and $\boldsymbol{r}(t)$ are the positions of the i-th planet and the spacecraft at epochs τ and t, respectively. Since the distance traveled by the light between the two epochs is $\rho = c(t-\tau)$, where c is the speed of light, the beacon relative position vector can be rewritten as

$$\boldsymbol{\rho}(t,\tau) = \rho\hat{\boldsymbol{\rho}} = c(t-\tau)\hat{\boldsymbol{\rho}} \tag{4}$$

From Fig. 2, note that $\rho = ||\boldsymbol{r}_i - \boldsymbol{r}||$, which is also equal to $c(t-\tau)$. Enforcing this equality yields to the following constraint functional

$$\mathcal{L} = c(t-\tau) - ||\boldsymbol{r}_i(\tau) - \boldsymbol{r}(t)|| = 0 \tag{5}$$

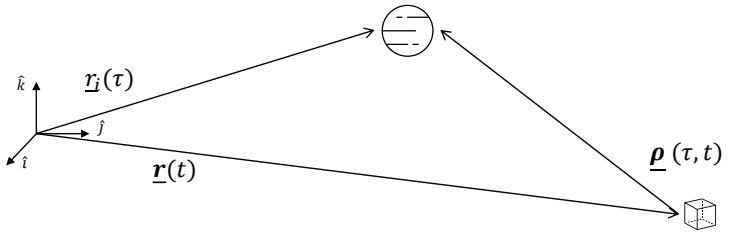

Fig. 2 Graphical representation of the light-time effect.

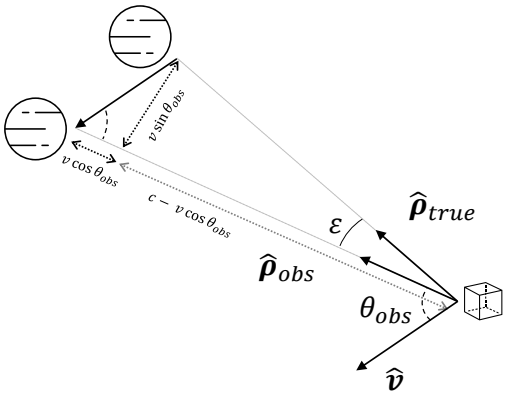

Fig. 3 Graphical representation of the celestial aberration.

The correction of the light-time effect is performed right after the propagation steps of the Kalman filter by solving Eq. (5) for τ. By knowing the spacecraft time t, the estimated spacecraft position, and the observed planet identifier, τ is found through the application of Newton–Raphson's method. The spacecraft time t is adopted as initial guess. Once τ is determined, it is exploited to retrieve the ephemerides of the observed planet at the epoch of light emission $\boldsymbol{r}_i(\tau)$, so correcting for the light-time effect.

C. Celestial Aberration

The celestial aberration matters whenever the observer velocity to the target is not negligible, as in the case of a probe moving in the Solar System. To account for this, a correction is performed every time a new observation is acquired, and before the estimation is measurement-updated. The procedure followed for the correction is the one described in [20].

With reference to Fig. 3, let θ_{obs} be the angle between the observed LoS $\hat{\boldsymbol{\rho}}_{\text{obs}}$ and the estimated unitary velocity vector of the probe $\hat{\boldsymbol{v}}$; i.e.,

$$\tan\theta_{\text{obs}} = \frac{||\hat{\boldsymbol{\rho}}_{\text{obs}} \times \hat{\boldsymbol{v}}||}{\hat{\boldsymbol{\rho}}_{\text{obs}}^{\top}\hat{\boldsymbol{v}}} \tag{6}$$

Then, the aberration angle ε is computed as

$$\tan\varepsilon = \frac{(v/c)\sin\theta_{\text{obs}}}{1-(v/c)\cos\theta_{\text{obs}}} \tag{7}$$

and the true LoS $\hat{\boldsymbol{\rho}}_{\text{true}}$ is retrieved such that

$$\hat{\boldsymbol{\rho}}_{\text{true}} = \frac{\hat{\boldsymbol{\rho}}_{\text{obs}}\sin\theta_{\text{true}} - \hat{\boldsymbol{v}}\sin\varepsilon}{\sin\theta_{\text{obs}}} \tag{8}$$

with $\theta_{\text{true}} = \theta_{\text{obs}} + \varepsilon$.

If the correction in Eq. (8) is neglected, the planet apparent position in the star tracker Field of View (FoV)

will appear as shifted to the real one. In particular, this error has a consistent impact on the estimation of the probe state in deep space [21]. Indeed, the estimation is more and more affected by the celestial aberration and by the light-time effect when the probe velocity and distance to the observed object increase, respectively.

D. Optimal Planets Selection Strategy

When estimating the probe position, it is beneficial to track those planets that will yield the highest accuracy possible in state determination. This is known as optimal beacons selection strategy. The approach followed for the selection of the most suitable pair of navigation planets is the one in [18], which is here implemented directly into the filter. It works by taking as input the estimated position of the spacecraft and the planets ephemerides, and returns the optimal pair of planets to be tracked. At first, the planets observability is assessed. Then, the pair of planets that yields the highest solution accuracy is selected.

1. Planets Observability

The Solar Aspect Angle (SAA) and the apparent magnitude are exploited to assess the visibility of a planet throughout the CubeSat interplanetary transfer. Only the planets whose SAA and apparent magnitude pass the threshold values imposed by the star tracker can be considered available for tracking.

The planet SAA (β in Fig. 1) is computed as

$$\beta = \text{acos}\left(\frac{-\boldsymbol{r}^\top \boldsymbol{\rho}}{||\boldsymbol{r}||\ ||\boldsymbol{\rho}||}\right) \tag{9}$$

When $\beta > \beta_{\text{min}}$, the beacon can be detected by the camera (provided sufficient beacon brightness), with β_{min} the threshold value imposed by the sensor specifications on the minimum SAA.

The apparent magnitude of a planet is the measure of its brightness viewed by an observer, which in this case is the spacecraft, and depends on the beacon absolute magnitude and on its distance to the probe and to the Sun. The values of the absolute magnitude M of the planets in the Solar System are reported in Table 1. Note that the absolute magnitude M can be also expressed as a function of the planet diameter and geometric albedo [27].

Table 1 Absolute magnitude of the planets of the Solar System [28]

Planet	Mer.	Ven.	Ear.	Mar.	Jup.	Sat.	Ura.	Nep.
M	-0.613	-4.384	-3.99	-1.601	-9.395	-8.914	-7.110	-7

By knowing the absolute magnitude and the estimated position of the spacecraft, the apparent magnitude m of the planets is computed. First, the phase angle (α in Fig. 1) is evaluated following the same approach of

Eq. (9). Then, the phase integral $q(\alpha)$, whose value depends on the reflecting surface properties, is defined. Since the planets can be approximated as ideal diffuse reflective spheres, the phase integral is [29]

$$q(\alpha) = \frac{2}{3}\left((1 - \frac{\alpha}{180})\cos\alpha + \frac{1}{\pi}\sin\alpha\right) \tag{10}$$

and the apparent magnitude is found by applying the following equation

$$m = M + 5\log_{10}\left(\frac{||\boldsymbol{\rho}||\ ||\boldsymbol{r}_{\text{pl}}||}{d_0^2}\right) - 2.5\log_{10} q(\alpha) \tag{11}$$

where d_0 is the reference distance equal to 1 AU. The correction term $-2.5\log_{10} q(\alpha)$ can be approximated employing more sophisticated models [28], which would enhance the apparent magnitude determination. When $m < m_{\text{max}}$ the planet can be detected by the camera, with m_{max} the threshold value set by the camera specifications on the maximum apparent magnitude.

2. Optimal Planets Selection

The solution accuracy of Eq. (2) is different for each pair of observed planets, owing to the problem geometry. Thus, to obtain the best navigation solution accuracy, the optimal pair of beacons needs to be found among the ones available. The procedure followed is the one presented in [18], in which the optimal pair of planets is selected by minimizing the figure of merit $\mathcal{J}$. The latter represents the trace of the solution error covariance matrix in Eq. (2) when considering perturbed line-of-sight directions. While the complete derivation can be found in [18], its definition is reported hereinafter:

$$\mathcal{J} = \sigma_{\text{str}}^2\ \frac{1+\cos\gamma^2}{\sin\gamma^4}\ \boldsymbol{d}^\top\ \left((\boldsymbol{I}_{3x3} - \hat{\boldsymbol{\rho}}_i\hat{\boldsymbol{\rho}}_i^\top) + (\boldsymbol{I}_{3x3} - \hat{\boldsymbol{\rho}}_j\hat{\boldsymbol{\rho}}_j^\top)\right)\boldsymbol{d} \tag{12}$$

where $\hat{\boldsymbol{\rho}}_i$ and $\hat{\boldsymbol{\rho}}_j$ are the unitary LoS vectors to the i-th and j-th planet, respectively, and σ_{str} is the standard deviation of the LoS angular error from the star tracker. Whereas, $\boldsymbol{d}$ and γ are defined as (see Fig. 1 for the latter)

$$\boldsymbol{d} = \boldsymbol{r}_i - \boldsymbol{r}_j \qquad\qquad \gamma = \text{acos}\left(\hat{\boldsymbol{\rho}}_i\hat{\boldsymbol{\rho}}_j\right) \tag{13}$$

where $\boldsymbol{d}$ is divided by 1 AU to keep $\mathcal{J}$ non-dimensional.

Note that $\mathcal{J}$ depends on both the observation problem and on the measurements uncertainty σ_{str}. Assuming that σ_{str} is the same for all the observations, since they are acquired with the same optical sensor, the problem of obtaining the best solution accuracy in Eq. (2) is traced back to the selection of the observation geometry that minimizes the figure of merit $\mathcal{J}$, and so the solution uncertainty. In particular, $\mathcal{J}$ is inversely

proportional to the fourth power of the sin γ and proportional to the distances of the planets. Thus, the optical beacons would be those planets close to the observer and whose γ is mostly near to $\frac{\pi}{2}$. The reader can refer to [18] for further details. A similar result can be found in [19] when the pseudo target strategy is adopted to select the asteroids targets.

III. Kalman Filter Implementation

This section deals with the setup of a dynamic estimation filter embedding the LoS measurements of planets in deep space. Sections III.A and III.B present the filter dynamics and measurement models, Sec. III.C its initialization, and Secs. III.D and III.E report comparisons for filter enhancements.

A. Dynamics Model

The process state $\boldsymbol{x}$ is defined as

$$\boldsymbol{x}(t) = [\boldsymbol{r}(t), \boldsymbol{v}(t), \boldsymbol{\eta}(t)]^\top \tag{14}$$

where $\boldsymbol{r}$ and $\boldsymbol{v}$ are the inertial probe position and velocity, respectively, and $\boldsymbol{\eta}$ is a vector of Gauss–Markow (GM) processes accounting for unmodeled terms: a 3-dimensional residual accelerations $\boldsymbol{\eta}_\mathrm{R}$ and the stochastic component of the Solar Radiation Pressure (SRP) $\boldsymbol{\eta}_\mathrm{SRP}$; that is, $\boldsymbol{\eta} = [\boldsymbol{\eta}_\mathrm{R}, \boldsymbol{\eta}_\mathrm{SRP}]^\top$.

The process is modeled using the following equation of motion

$$\dot{\boldsymbol{x}}(t) = \boldsymbol{f}(\boldsymbol{x}(t), t) + \boldsymbol{w} \tag{15}$$

where $\boldsymbol{f}$ is the vector field embedding the deterministic part, while $\boldsymbol{w}$ is the process white noise

$$\boldsymbol{f} \coloneqq \begin{bmatrix} \boldsymbol{v} \\ -\mu_\mathrm{Sun}\dfrac{\boldsymbol{r}}{r^3} + C_\mathrm{R}\dfrac{P_0 R_0^2}{c}\dfrac{A_\mathrm{s}}{m_\mathrm{s}}\dfrac{\boldsymbol{r}}{r^3} \\ -\xi\boldsymbol{\eta}_\mathrm{R} \\ -\xi\boldsymbol{\eta}_\mathrm{SRP} \end{bmatrix} \qquad \boldsymbol{w} = \begin{bmatrix} \boldsymbol{0}_{3x1} \\ \boldsymbol{\eta}_\mathrm{R} + \boldsymbol{\eta}_\mathrm{SRP} \\ \boldsymbol{w}_\mathrm{R} \\ \boldsymbol{w}_\mathrm{SRP} \end{bmatrix} \tag{16}$$

The SRP is described using the cannonball model [30]: C_R is the coefficient of reflection, P_0 the solar power, R_0 the Sun radius, A_s the cross section area of the probe, and m_s its mass. Since the spacecraft is on an interplanetary transfer, third-body perturbations can be neglected [8]. In the Langevin equations

$$\dot{\boldsymbol{\eta}}_\mathrm{R} = -\xi\boldsymbol{\eta}_\mathrm{R} + \boldsymbol{w}_\mathrm{R} \qquad\qquad \dot{\boldsymbol{\eta}}_\mathrm{SRP} = -\xi\boldsymbol{\eta}_\mathrm{SRP} + \boldsymbol{w}_\mathrm{SRP} \tag{17}$$

the coefficient ξ defines the reciprocal of the correlation time, while $\boldsymbol{w}_{\mathrm{R}}$ and $\boldsymbol{w}_{\mathrm{SRP}}$ are the process noises of the GM parameters with σ_{R} and σ_{SRP} standard deviations, respectively [31].

The Jacobian matrix $\boldsymbol{F} \coloneqq \partial \boldsymbol{f}/\partial \boldsymbol{x}$ is a 12×12 matrix defined as

$$\boldsymbol{F} = \begin{bmatrix} \boldsymbol{0}_{3x3} & \boldsymbol{I}_{3x3} & \boldsymbol{0}_{3x3} & \boldsymbol{0}_{3x3} \\ -\left(\mu_{\mathrm{Sun}} + C_{\mathrm{R}} \dfrac{P_0 R_0^2}{c} \dfrac{A_{\mathrm{s}}}{m_{\mathrm{s}}}\right) \dfrac{\boldsymbol{I} r^2 + 3\boldsymbol{r}\boldsymbol{r}^{\top}}{r^5} & \boldsymbol{0}_{3x3} & \boldsymbol{0}_{3x3} & \boldsymbol{0}_{3x3} \\ \boldsymbol{0}_{3x3} & \boldsymbol{0}_{3x3} & -\xi \boldsymbol{I}_{3x3} & \boldsymbol{0}_{3x3} \\ \boldsymbol{0}_{3x3} & \boldsymbol{0}_{3x3} & \boldsymbol{0}_{3x3} & -\xi \boldsymbol{I}_{3x3} \end{bmatrix} \tag{18}$$

The covariance matrix of the process noise $\boldsymbol{w}$ in Eq. (16) is

$$\boldsymbol{Q} = \mathrm{diag}(\boldsymbol{0}_{3x3}, \boldsymbol{Q}_A, \boldsymbol{Q}_{\mathrm{R}}, \boldsymbol{Q}_{\mathrm{SRP}}) \tag{19}$$

with $\boldsymbol{Q}_{\mathrm{R}} = \sigma_{\mathrm{R}}^2 \boldsymbol{I}_{3x3}$, $\boldsymbol{Q}_{\mathrm{SRP}} = \sigma_{\mathrm{SRP}}^2 \boldsymbol{I}_{3x3}$, and $\boldsymbol{Q}_{\mathrm{A}} = (\boldsymbol{Q}_{\mathrm{R}} + \boldsymbol{Q}_{\mathrm{SRP}})/(2\xi)$.

B. Measurement model

The relative direction of the navigation beacon as seen by the probe $\hat{\boldsymbol{\rho}}$ is defined by two angles that represent the planet location in the camera FoV: the Azimuth (Az) and the Elevation (El). The measurement model equation is so defined as

$$\boldsymbol{h} = \begin{bmatrix} Az \\ El \end{bmatrix} = \begin{bmatrix} \arctan\left(\dfrac{\hat{\rho}_y}{\hat{\rho}_x}\right) \\ \arcsin(\hat{\rho}_z) \end{bmatrix} \tag{20}$$

where $\hat{\rho}_x$, $\hat{\rho}_y$ and $\hat{\rho}_z$ are the components of the LoS unit vector. These are found by applying the light-time correction procedure described in Sec. II.B at the end of the propagation steps: first, the parameter τ is found by solving Eq. (5); then, τ is exploited to determine the ephemerides of the observed planet. Finally, the corrected planet LoS direction is retrieved by solving Eq. (3).

Additionally, at a given epoch t_k, the observed vector $\boldsymbol{y}_{\mathrm{obs}}$ is a 2-dimensional vector, as only one planet at a time is tracked. It is is modeled starting from $\boldsymbol{h}$ as

$$\boldsymbol{y}_{\mathrm{obs}} = \bar{\boldsymbol{y}}_{\mathrm{obs}} + \boldsymbol{\nu} = \underbrace{\boldsymbol{h}(\boldsymbol{x}_k) + \boldsymbol{\Delta}_{\mathrm{aber}}}_{\bar{\boldsymbol{y}}_{\mathrm{obs}}} + \underbrace{3\sigma_{\mathrm{str}} \boldsymbol{k}}_{\boldsymbol{\nu}} \tag{21}$$

where $\bar{\boldsymbol{y}}_{\mathrm{obs}}$ is the unperturbed observed vector and $\boldsymbol{\nu}$ the measurement white noise. More specifically, $\boldsymbol{x}_k$ is the probe state at t_k, $\boldsymbol{\Delta}_{\mathrm{aber}}$ the vector that introduces the celestial aberration error (see Sec. II.C), σ_{str} the standard deviation of the LoS angular error from the star tracker (considered equal for both the azimuth and

the elevation), and $\boldsymbol{k}$ a white noise vector with values within $[-1; 1]$. The correction of the celestial aberration is applied inside the filter, as shown in Sec. II.C. Once $\hat{\boldsymbol{\rho}}_{\text{true}}$ is found, $\boldsymbol{y}_{\text{true}}$ can be evaluated applying Eq. (20) and employed to define the innovation term.

To implement the correction block (see Table 2), the Jacobian matrix $\boldsymbol{H} = \partial \boldsymbol{h} / \partial \boldsymbol{x}$ is needed. To simply the notation, let $\hat{\boldsymbol{\rho}} = \hat{\boldsymbol{\rho}}_i$; then

$$\boldsymbol{H}_i = \begin{bmatrix} \dfrac{1}{1+\left(\dfrac{\hat{\rho}_y}{\hat{\rho}_x}\right)^2} \dfrac{\hat{\rho}_y}{\hat{\rho}_x^2 \rho} & \dfrac{-1}{1+\left(\dfrac{\hat{\rho}_y}{\hat{\rho}_x}\right)^2} \dfrac{1}{\hat{\rho}_x \rho} & 0 & \mathbf{0}_{1x3} & \mathbf{0}_{1x6} \\ \dfrac{1}{\sqrt{1-\hat{\rho}_z^2}} \dfrac{\hat{\rho}_x \hat{\rho}_z}{\rho} & \dfrac{1}{\sqrt{1-\hat{\rho}_z^2}} \dfrac{\hat{\rho}_y \hat{\rho}_z}{\rho} & \dfrac{1}{\sqrt{1-\hat{\rho}_z^2}} \dfrac{-1+\hat{\rho}_z^2}{\rho} & \mathbf{0}_{1x3} & \mathbf{0}_{1x6} \end{bmatrix} \tag{22}$$

The measurement noise has zero mean and is uncorrelated to $\boldsymbol{w}$. Its covariance matrix $\boldsymbol{R}$ is a 2×2 matrix since it is referred to one beacon at a time. Its coefficients can be obtained by means of the standard deviation error of the instrument used for the observations. The star tracker error is assumed to be common to all the components of the matrix $\boldsymbol{R}$, and the latter can be expressed such that

$$\boldsymbol{R} = \sigma_{\text{str}}^2 \boldsymbol{I} \tag{23}$$

C. Filter Initialization

The initialization of the filter is performed by sampling the initial state vector $\boldsymbol{x}_0$ with mean $\tilde{\boldsymbol{x}}_0$ and covariance matrix $\boldsymbol{P}_0$. The latter is defined as follows

$$\boldsymbol{P}_0 = \text{diag}(\sigma_{\text{r}}^2 \boldsymbol{I}_{3x3}, \sigma_{\text{v}}^2 \boldsymbol{I}_{3x3}, \sigma_{\text{R}}^2 \boldsymbol{I}_{3x3}, \sigma_{\text{SRP}}^2 \boldsymbol{I}_{3x3}) \tag{24}$$

where σ_{r} and σ_{v} are the initial standard deviations of the position and velocity, respectively. The initial state is then computed by applying the 3σ standard deviation rule, i.e.,

$$\boldsymbol{x}_0 = \tilde{\boldsymbol{x}}_0 + 3\sqrt{\boldsymbol{P}_0}\boldsymbol{k} \tag{25}$$

where $\boldsymbol{k}$ is a random vector with values are within $[-1; 1]$, and the square root operates on the elements of $\boldsymbol{P}_0$.

D. Standard Filtering Strategy

In the standard filtering strategy, the batch EKF filter is used for the measurement update [32], whereas the state error covariance matrix $\boldsymbol{P}$ is employed to determine the state uncertainty. The implemented scheme is reported in Table 2: $\boldsymbol{x}_{p_k}$ is the predicted state vector with error covariance matrix $\boldsymbol{P}_{p_k}$, $\boldsymbol{K}_k$ the Kalman gain, $\boldsymbol{x}_{c_k}$ the corrected state vector with error covariance matrix $\boldsymbol{P}_{c_k}$ and $\boldsymbol{\Phi}_k$ the state transition matrix.

Table 2 Standard filtering strategy

System State Space	$\dot{\boldsymbol{x}} = \boldsymbol{f}(\boldsymbol{x}(t), t) + \boldsymbol{w}$		Eq. (16)
	$\boldsymbol{y}_k = \boldsymbol{h}(\boldsymbol{x}_k) + \boldsymbol{\nu}_k$		Eq. (20)
Propagation Block	$\boldsymbol{x}_{p_k} = \boldsymbol{x}_{c_{k-1}} + \int_{t_{k-1}}^{t_k} \boldsymbol{f}(\boldsymbol{x}(t), t)\mathrm{d}t$	$\boldsymbol{x}_{c_0} = E[\boldsymbol{x}_0]$	Eq. (25)
	$\boldsymbol{\Phi}_k = \boldsymbol{\Phi}_{k-1} + \int_{t_{k-1}}^{t_k} \boldsymbol{F}\boldsymbol{\Phi}\mathrm{d}t$	$\boldsymbol{\Phi}_0 = \boldsymbol{I}$	
	$\boldsymbol{S}_k = \boldsymbol{S}_{k-1} + \int_{t_{k-1}}^{t_k} \boldsymbol{\Phi}\boldsymbol{Q}\boldsymbol{\Phi}^\top\mathrm{d}t$	$\boldsymbol{S}_0 = \boldsymbol{Q}$	Eq. (19)
	$\boldsymbol{P}_{p_k} = \boldsymbol{\Phi}_k \boldsymbol{P}_{c_k} \boldsymbol{\Phi}_k^\top + \boldsymbol{S}_k$	$\boldsymbol{P}_{c_0} = E[\boldsymbol{x}_0 \boldsymbol{x}_0^\top]$	Eq. (24)
Correction Block	$\boldsymbol{K}_k = \boldsymbol{P}_{p_k}\boldsymbol{H}_k^\top(\boldsymbol{H}_k\boldsymbol{P}_{p_k}\boldsymbol{H}_k^\top + \boldsymbol{R}_k)^{-1}$		
	$\boldsymbol{x}_{c_k} = \boldsymbol{x}_{p_k} + \boldsymbol{K}_k[\boldsymbol{y}_k - \boldsymbol{h}(\boldsymbol{x}_{p_k})]$		
	$\boldsymbol{P}_{c_k} = (\boldsymbol{I} - \boldsymbol{K}_k\boldsymbol{H}_k)\boldsymbol{P}_{p_k}(\boldsymbol{I} - \boldsymbol{K}_k\boldsymbol{H}_k)^\top + \boldsymbol{K}_k\boldsymbol{R}_k\boldsymbol{K}_k^\top$		

E. Alternative Filtering Techniques

Since the goal of this work consists of deploying the orbit determination algorithm on a CubeSat representative platform, the numerical stability of the filter needs to be investigated to avoid the rise of numerical issues after the implementation on hardware [31]. To tackle these problems, alternative formulations of the standard filtering strategy are applied to both the time and the measurement update steps, which will result in the implementation of four additional alternative filtering schemes. Differently from the standard scheme, three of the new approaches exploit the sequential measurement update method. This one carries out the correction of the estimation without matrix inversion by processing the measurements once at a time. This helps saving computational time and memory, and is a desirable formulation for embedded systems with no matrix libraries [32]. Moreover, factorization methods are exploited for the solution time-update.

1. Method A

Method A employs Potter's equation for processing the measurements, and the Householder algorithm for the square root matrix time propagation [32]. The core procedure of Method A consists of the complete replacement of the matrix $\boldsymbol{P}$ with its square-root matrix $\mathcal{S}$, which is numerically more stable due to the halving of the conditioning number. The decomposition of the matrix $\boldsymbol{P}$ is performed only once at the beginning of the filtering procedure by applying the Cholesky factorization. Subsequently, the Householder's algorithm is employed inside the filter propagation block, whereas Potter's equation manages the observation in the correction part [32]. The flowchart of the Householder algorithm, which is adopted for the square-root matrix time-update, is illustrated in Fig. 4.

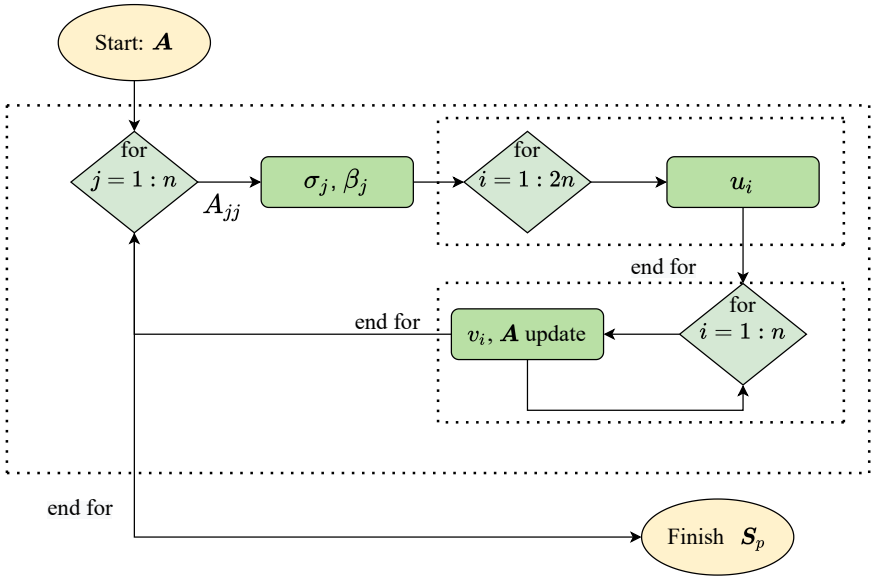

Fig. 4 Flowchart of the Householder algorithm

At first, the matrix $\boldsymbol{A}$ at t_k needs to be defined such that

$$\boldsymbol{A}^{(k)} = \begin{bmatrix} \mathcal{S}_c^{\top(k)} \boldsymbol{\Phi}^{\top(k)} \\ \sqrt{\boldsymbol{S}^{\top(k)}} \end{bmatrix} \tag{26}$$

where $\mathcal{S}_c$ is the square root matrix coming from the previous measurement update, while $\boldsymbol{S}$ and $\boldsymbol{\Phi}$ are defined in Table 2. Note that from now on the superscript (k) will be omitted for easing the treatment.

By reminding that the parameter n represents the dimension of the state vector, the first for loop is implemented. The two scalars σ_j and β_j are evaluated as follows:

$$\sigma_j = \text{sign}(A_{jj}) \sqrt{\sum_{i=j}^{2n} A_{ij}^2} \qquad\qquad \beta_j = \frac{1}{\sigma_j (\sigma_j + A_{jj})} \tag{27}$$

Then, the vector $\boldsymbol{u}$ and $\boldsymbol{v}$ are obtained by entering into the first and second for sub-loops, respectively, and by applying:

$$u_i = \begin{cases} 0 & i < j \\ \sigma_j + A_{jj} & i = j \\ A_{ij} & i > j \end{cases} \qquad v_i = \begin{cases} 0 & i < j \\ 1 & i = j \\ \beta_j \boldsymbol{u}^\top \boldsymbol{A}(:, i) & i > j \end{cases} \tag{28}$$

The matrix $\boldsymbol{A}$ is time-updated in the second for sub-loop as $\boldsymbol{A}^{(k+1)} = \boldsymbol{A} - \boldsymbol{u}\boldsymbol{v}^\top$. Finally, the procedure ends

with the definition of the a-priori square root matrix $\mathcal{S}_p$ at the epoch t_{k+1} such that $\mathcal{S}_p^{(k+1)} = \boldsymbol{A}(1:n,:)^\top$. Once $\mathcal{S}_p^{(k+1)}$ is evaluated, the Potter's square root measurement-update equation is employed for obtaining the matrix $\mathcal{S}_c^{(k+1)}$. The flowchart of the procedure is reported in Fig. 5. Note that the superscript $(k+1)$ is omitted to ease the discussion, and the parameter r represents the number of measurements at each epoch.

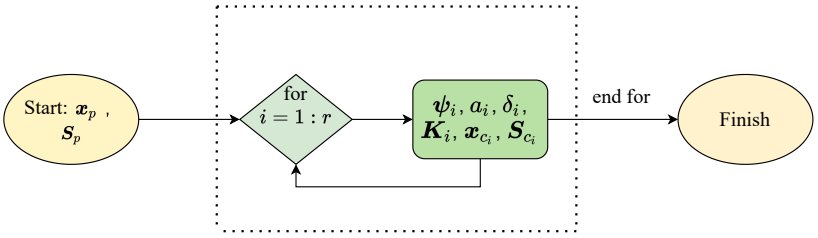

Fig. 5 Flowchart of Potter's measurement-update procedure

At first, the procedure is initialized: 1) $\mathcal{S}_{c_0} = \mathcal{S}_p$ and 2) $\boldsymbol{x}_{c_0} = \boldsymbol{x}_p$. Then, at each cycle of the for loop, the parameters are evaluated as follows:

$$\begin{cases} \boldsymbol{\psi}_i = \mathcal{S}_{c_{i-1}}^\top \boldsymbol{H}_i^\top \\ a_i = \dfrac{1}{\boldsymbol{\psi}_i^\top \boldsymbol{\psi}_i + R_{ii}} \\ \delta_i = \dfrac{1}{1 + \sqrt{a_i + R_{ii}}} \\ \boldsymbol{K}_i = a_i \mathcal{S}_{c_{i-1}} \boldsymbol{\psi}_i \\ \boldsymbol{x}_{c_i} = \boldsymbol{x}_{c_{i-1}} + \boldsymbol{K}_i \left(\boldsymbol{y}_i - h(\boldsymbol{x}_{c_{i-1}}) \right) \\ \mathcal{S}_{c_i} = \mathcal{S}_{c_{i-1}} - \delta_i \boldsymbol{K}_i \boldsymbol{\psi}_i^\top \end{cases} \tag{29}$$

where $\boldsymbol{H}_i$ is the i-esimal row of $\boldsymbol{H}$, R_{ii} the variance of the i-esimal measurement, $\boldsymbol{K}_i$ the Kalman gain, while $\mathcal{S}_{c_i}$ and $\boldsymbol{x}_{c_i}$ the square root matrix and the state vector, respectively, after the i-esimal measurement is processed.

2. Method B

Method B implements the UDU filtering scheme, in which the upper triangular matrix $\boldsymbol{U}$ and the diagonal matrix $\boldsymbol{D}$ are propagated. The UDU factorization is adopted to enhance the numerical precision of the matrix $\boldsymbol{P}$. Differently from the square root method, the UDU factorization needs to be performed at each measurement update. The observations are then processed employing a sequential algorithm [32]. To

propagate $\boldsymbol{U}$ and $\boldsymbol{D}$, firstly, the matrices $\boldsymbol{W}$ and $\hat{\boldsymbol{D}}$ are defined as

$$\boldsymbol{W} = \begin{bmatrix} \boldsymbol{\Phi}^{(k+1)}\boldsymbol{U}_c^{(k)} & \boldsymbol{I}_{nxn} \end{bmatrix} \qquad \hat{\boldsymbol{D}} = \begin{bmatrix} \boldsymbol{D}_c^{(k)} & \boldsymbol{0}_{nxn} \\ \boldsymbol{0}_{nxn} & \boldsymbol{S}^{(k+1)} \end{bmatrix} \tag{30}$$

where $\boldsymbol{U}_c^{(k)}$ and $\boldsymbol{D}_c^{(k)}$ are retrieved from the previous measurement-update step. Then, the Gram-Schmidt orthogonalization procedure represented in Fig. 6 is applied.

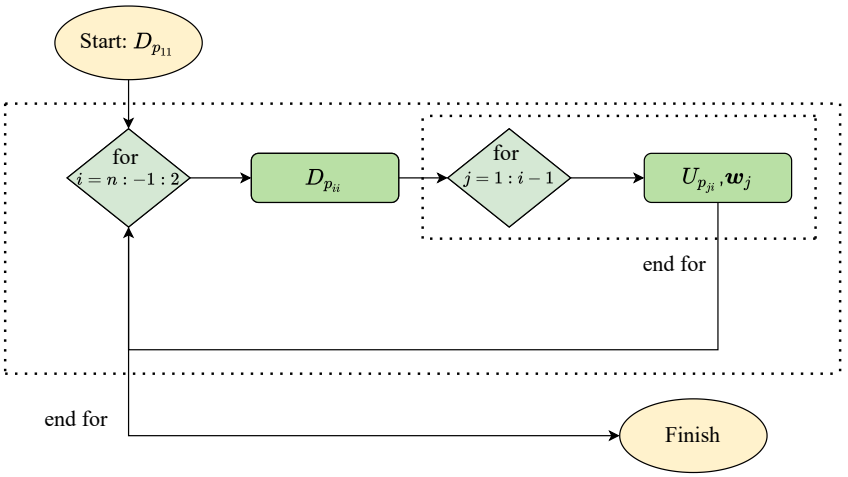

Fig. 6 Flowchart of Method B time-update procedure

The first element of $\boldsymbol{D}_p^{(k+1)}$ is evaluated as $D_{p_{11}}^{(k+1)} = \boldsymbol{w}_1^\top \hat{\boldsymbol{D}} \boldsymbol{w}_1$, where $\boldsymbol{w}_1$ represents the first column of $\boldsymbol{W}^\top$. In a similar way, the other elements of $\boldsymbol{D}_p^{(k+1)}$ are defined. Then, by entering into the second embedded for loop the elements of $\boldsymbol{U}_p$ are found, and the vector $\boldsymbol{w}_j$ is updated as

$$U_{p_{ji}}^{(k+1)} = \frac{\boldsymbol{w}_j^\top \hat{\boldsymbol{D}} \boldsymbol{w}_i}{D_{p_{ii}}^{(k+1)}} \qquad \boldsymbol{w}_j = \boldsymbol{w}_j - U_{p_{ji}}^{(k+1)} \boldsymbol{w}_i \tag{31}$$

In this way $\boldsymbol{U}_p^{(k+1)}$ and $\boldsymbol{D}_p^{(k+1)}$ are found. Taking as input the results of the time propagation, the measurement update is sequentially performed as illustrated in Fig. 7 [32].

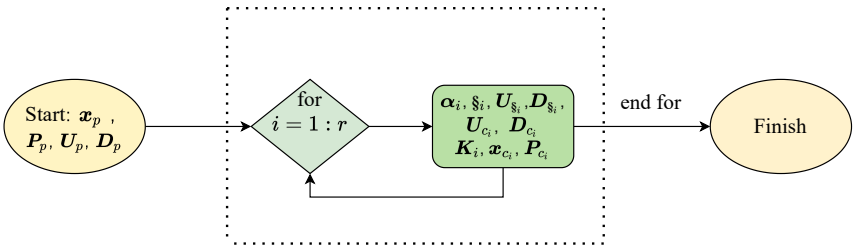

Fig. 7 Flowchart of the Method B measurement-update procedure

Let us omit the superscript $(k+1)$ over each element to ease the discussion. The procedure is initialized as: 1) $\boldsymbol{U}_{c_0} = \boldsymbol{U}_p$, 2)$\boldsymbol{D}_{c_0} = \boldsymbol{D}_p$, 3) $\boldsymbol{P}_{c_0} = \boldsymbol{P}_p = \boldsymbol{U}_p \boldsymbol{D}_p \boldsymbol{U}_p^\top$, and 4) $\boldsymbol{x}_{c_0} = \boldsymbol{x}_p$. Then, at each cycle of the for loop, the following parameters are evaluated as:

$$
\begin{cases}
\alpha_i = \boldsymbol{H}_i \, \boldsymbol{P}_{c_{i-1}} \, \boldsymbol{H}_i^\top + R_{ii} \\
\boldsymbol{\S}_i = \boldsymbol{D}_{c_{i-1}} - \dfrac{1}{\alpha_i} (\boldsymbol{D}_{c_{i-1}} \boldsymbol{U}_{c_{i-1}}^\top \boldsymbol{H}_i^\top) \, (\boldsymbol{D}_{c_{i-1}} \boldsymbol{U}_{c_{i-1}}^\top \boldsymbol{H}_i^\top)^\top \\
\boldsymbol{U}_{\boldsymbol{\S}_i} \boldsymbol{D}_{\boldsymbol{\S}_i} = \mathrm{UDUfact}(\boldsymbol{\S}_i) \\
\boldsymbol{U}_{c_i} = \boldsymbol{U}_{c_{i-1}} \boldsymbol{U}_{\boldsymbol{\S}_i} \\
\boldsymbol{D}_{c_i} = \boldsymbol{D}_{\boldsymbol{\S}_i} \\
\boldsymbol{P}_{c_i} = \boldsymbol{U}_{c_i} \boldsymbol{D}_{c_i} \boldsymbol{U}_{c_i}^\top \\
\boldsymbol{K}_i = \dfrac{\boldsymbol{P}_{c_i} \, \boldsymbol{H}_i^\top}{R_{ii}} \\
\boldsymbol{x}_{c_i} = \boldsymbol{x}_{c_{i-1}} + \boldsymbol{K}_i \left(\boldsymbol{y}_i - \boldsymbol{h}(\boldsymbol{x}_{c_{i-1}}) \right)
\end{cases}
\tag{32}
$$

where $\boldsymbol{H}_i$ is the i-esimal row of $\boldsymbol{H}$, R_{ii} the variance of the i-esimal measurement, $\boldsymbol{U}_{c_i}$, $\boldsymbol{D}_{c_i}$, $\boldsymbol{P}_{c_i}$ the measurement-updated covariance matrices after the i-esimal measurement is processed, and $\boldsymbol{U}_{\boldsymbol{\S}_i}$, $\boldsymbol{D}_{\boldsymbol{\S}_i}$ the matrices found by applying the UDU factorization to $\boldsymbol{\S}$.

3. Method C

A different approach that may improve the numerical stability of the estimator is achieved through the non-dimensionalization of the model equations. Indeed, by virtue of the Buckingham theorem, the validity of the physics laws does not depend on a particular unit system [33]. In Method C the standard filtering strategy is employed with non-dimensional model equations. As first step, the dimensional analysis of the variables that enter into the estimator needs to be performed. The dimensions of the components of the state vector are described only through two fundamental physical quantities: the length and the time. Thus, only a position $\bar{r}$

and an epoch $\bar{t}$ parameter are needed to non-dimensionalized the whole filtering procedure.

The dimensionless state vector $\bar{\boldsymbol{x}}$ and the equation of motion $\bar{\boldsymbol{f}}$ are defined as

$$\bar{\boldsymbol{x}} = \begin{bmatrix} \bar{\boldsymbol{r}} \\ \bar{\boldsymbol{v}} \\ \bar{\boldsymbol{\eta}}_{\mathrm{R}} \\ \bar{\boldsymbol{\eta}}_{\mathrm{SRP}} \end{bmatrix} = \begin{bmatrix} \boldsymbol{r}/\bar{r} \\ \boldsymbol{v}/(\bar{r}\bar{t}^{-1}) \\ \boldsymbol{\eta}_{\mathrm{R}}/(\bar{r}\bar{t}^{-2}) \\ \boldsymbol{\eta}_{\mathrm{SRP}}/(\bar{r}\bar{t}^{-2}) \end{bmatrix} \qquad \bar{\boldsymbol{f}} = \begin{bmatrix} \bar{\boldsymbol{v}} \\ \frac{\bar{t}^2}{\bar{r}^3}\left(-\mu_{\mathrm{Sun}} + C_{\mathrm{R}} \frac{P_0 R_0^2}{c} \frac{A_{\mathrm{s}}}{m_{\mathrm{s}}} \right) \frac{\bar{\boldsymbol{r}}}{||\bar{\boldsymbol{r}}||^3} \\ -\bar{t}\xi\bar{\boldsymbol{\eta}}_{\mathrm{R}} \\ -\bar{t}\xi\bar{\boldsymbol{\eta}}_{\mathrm{SRP}} \end{bmatrix} \tag{33}$$

and the same argument is applied for evaluating the dimensionless Jacobian matrices $\bar{\boldsymbol{F}}$ and $\bar{\boldsymbol{H}}$, and the covariance matrices $\bar{\boldsymbol{Q}}$, $\bar{\boldsymbol{R}}$ and $\bar{\boldsymbol{P}}_0$.

4. Method D

Method D is simply the non-dimensional version of Method A.

Table 3 reports the algorithms used for the implementation of the aforementioned techniques.

Table 3 Features of the alternative filtering technique

Method	Measurement update	Time update
A	Potter's equation (Sequential)	Householder algorithm (Propagation of $\mathcal{S}$)
B	Sequential scheme	Propagation of $\boldsymbol{U}$ and $\boldsymbol{D}$
C	Non-dimensional standard (batch) scheme	Non-dimensional propagation of $\boldsymbol{P}$
D	Non-dimensional Potter's equation	Non-dimensional Householder algorithm

IV. Results

A. Test Case Definition

In the study case, a CubeSat performs an interplanetary transfer toward Mars, during which it estimates its position and velocity by tracking the visible planets. At t_0, the probe nominal position and velocity are defined by the vectors $\tilde{\boldsymbol{r}}_0$ and $\tilde{\boldsymbol{v}}_0$, whose components are in Table 4 (J2000 ecliptic reference frame). Fig. 8 shows the nominal probe trajectory.

Table 4 Probe state at t_0 = 9832 [mjd2000]

	Position [km]	Velocity [km/s]
x	4.3936×10^7	-29.9208
y	1.4582×10^8	12.1815
z	1.4841×10^6	0.4364

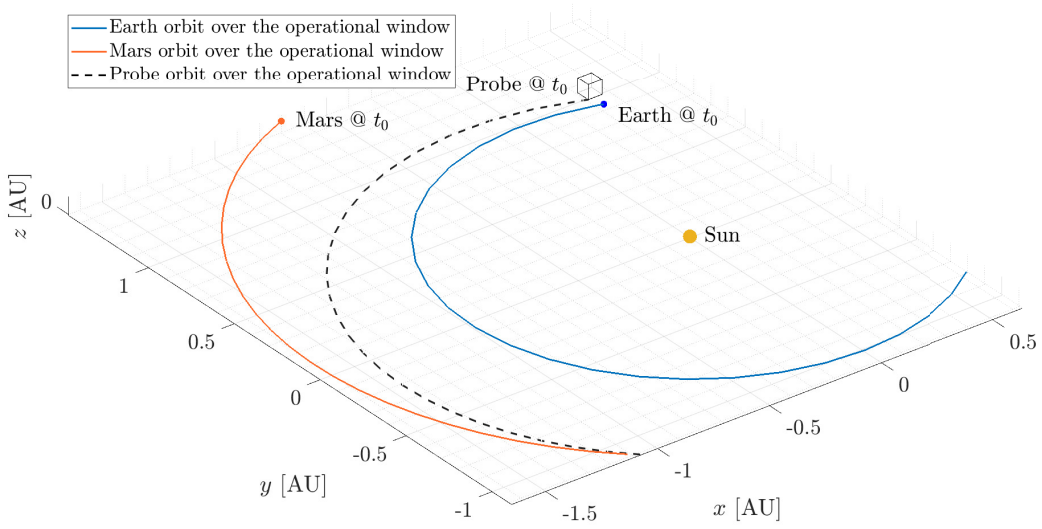

Fig. 8 Probe's trajectory (dashed line), departure and arrival planets (solid lines) during the operational window.

Starting from t_0, the estimation procedure begins. The probe tracks the first planet of the selected couple for one hour with a measurement frequency of 0.01 Hz, then it performs a slew maneuver of twenty minutes during which the state is only propagated (and thus not corrected). Then, the observations relative to the second planet are gathered for another hour, and, finally, the state is propagated for ten days. Therefore, only two hours every ten days are reserved for orbit determination purposes. The entire operational window is composed of 25 navigation legs of 10 days 2 hours and 20 minutes each, where the aforementioned navigation cycle is repeated recursively. The navigation cycle is outlined in Fig. 9.

Note that only the optimal pair of planets is tracked for each navigation leg. Indeed, when a limited time window is reserved for navigation and more than two planets are tracked, the filter performances worsen. This occurs because 1) the optimal couple that yields the smallest uncertainty region is tracked for short time, so preventing a proper estimation correction, 2) the uncertainty region created by another non-optimal couple

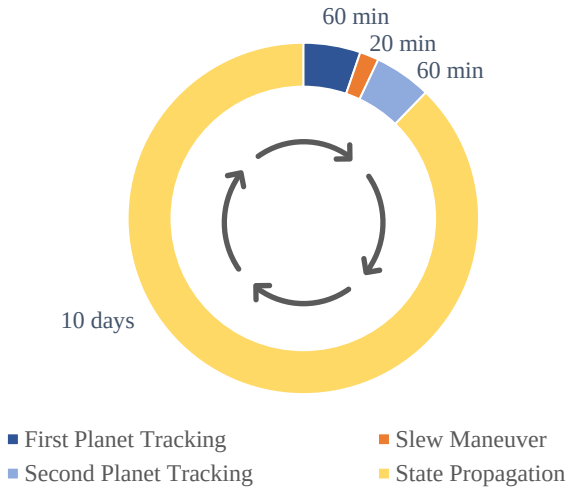

Fig. 9 Outline of the navigation cycle

is greater than the optimal one, hence tracking the third planet will not improve the estimation compared to the optimal one. Additionally, the higher is the number of observed planets, the higher will be the number of slew maneuvers required to point them, and thus the longer will be the time not allocated to the correction of the estimation.

1. Planets Observability

It is assumed that the imaging instrument can observe planets characterized by relative magnitude lower than 6 with SAA greater than 35 deg. This comes from typical performances of star trackers for CubeSats[†]. Planets not complying with these thresholds are not accounted for in the specific navigation campaign. Fig. 10 shows the profile of the planets SAA and apparent magnitude over the operational window. It can be noticed that Mercury is always not available due to its vicinity to the Sun (SAA $<$ 35 deg for the considered deep-space orbit), whereas Uranus and Neptune are never seen because of their faint luminosity ($m > 6$).

2. Optimal Planets Selection

Once the observability of the planets is assessed, the optimal planets selection strategy is performed. The procedure consists of finding the pair of planets among the ones available that minimizes the figure of merit $\mathcal{J}$ in Eq. (12). The strategy is embedded in the estimator, and it is implemented at the beginning of each navigation leg. Indeed, since the planets observation lasts only two hours, it is reasonable to assume that the selected pair of planets preserves its optimality throughout each navigation window. The optimal planets are reported in Fig. 11, where the black dots represent the values of $\mathcal{J}$ and γ for the selected optimal couple at the beginning of each navigation leg.

[†]`https://www.cubesatshop.com/`, last visited on June 2021

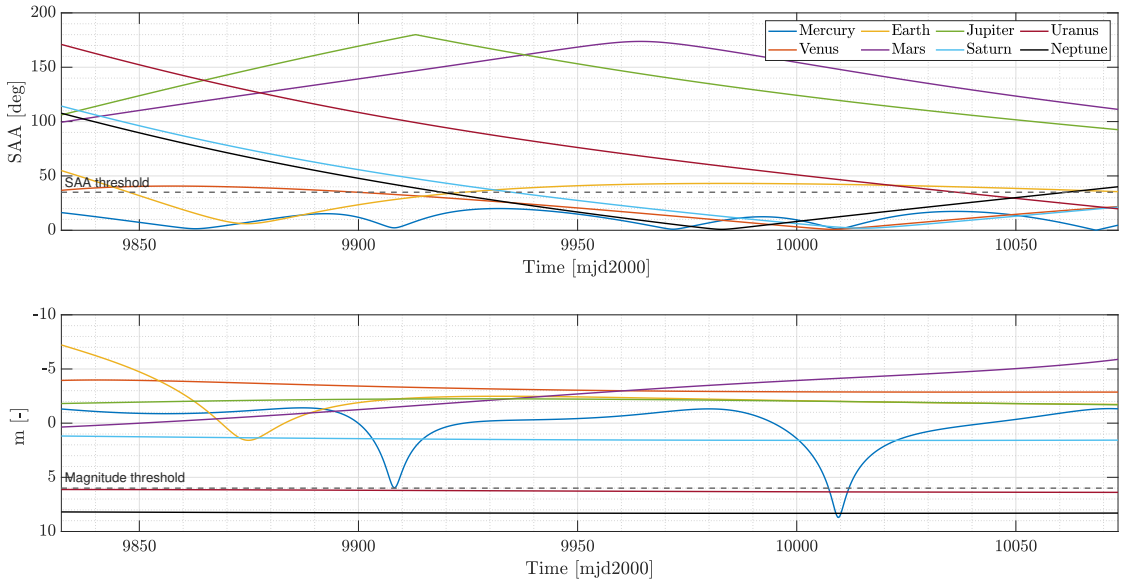

Fig. 10 Planets Solar Aspect Angle (SAA) and apparent magnitude (m) over the CubeSat trajectory. The dashed lines represent the assumed thresholds.

3. Planets Resolvability

To verify the suitability of the celestial triangulation as navigation technique in deep space, the planets resolvability is analyzed. To this aim, the Object-to-Pixel Ratio (OPR) of each planet is evaluated. The OPR can be seen as a qualitative factor that represents an initial knowledge about the dimension in pixel that a planet would have on the imager without considering defocusing and noises of the camera and the environment.

The Object to Pixel Ratio (OPR) is defined as

$$\mathrm{OPR} = 2\arctan\left(\frac{R_\mathrm{p}}{\rho}\right)\frac{N_\mathrm{px}}{FOV} \tag{34}$$

where R_p is the planet mean radius and N_px the number of camera pixels. The OPR of the exploited planets is computed considering the sensor FOV equal to 20 deg and N_px of 1024. When OPR < 1, planets apparent dimensions are lower than a pixel: they are not resolved, but sub-pixel accuracy in the LoS measurement can be reached by defocusing the light on the imager [17]. As Fig. 12 shows, Earth and Mars are resolved in the first and last part of the transfer orbit, respectively. Also in these circumstances, to increase the centroid precision, light defocusing is applied.

B. Performances

The characteristics of the star tracker considers $3\sigma_\mathrm{str}$ equal to 15 arcsec. This comes as a contribution due to attitude determination (9 arcseconds [25]), planet centroiding error (3.5 arcseconds), and a small margin

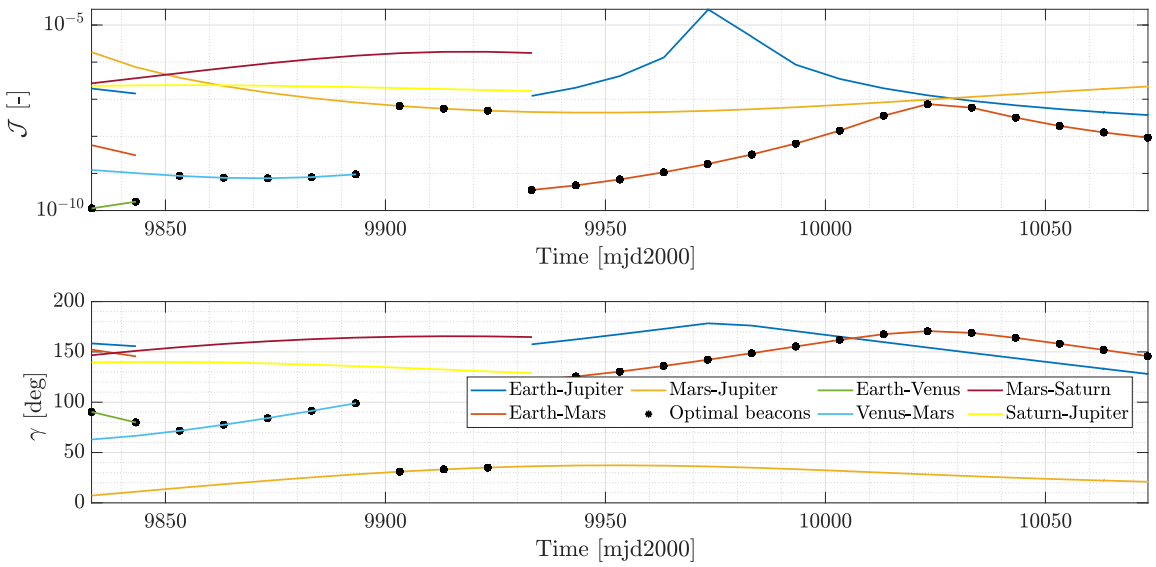

Fig. 11 $\mathcal{J}$ and γ trends over the operational window for the combinations of available planets. The optimal selection is represented with black dots.

due to unmodelled effects such as thermoelastic deformations of the spacecraft (2.5 arcseconds). The initial standard deviations of the state are reported in Table 5.

Table 5 Accuracy of the state components at t_0

σ_{r} [km]	σ_{v} [km/s]	σ_{SRP} [km/s^2]	σ_{R} [km/s^2]
10^4	10^{-1}	10^{-12}	10^{-12}

Note that the values are selected following a conservative approach, taking into account that in deep space the initial position and velocity are usually known with an accuracy better than 10000 km and 0.1 km/s, respectively. In addition, a study is performed to evaluate the threshold value of the position initial standard deviation over which the orbit determination algorithm is not able to select the optimal targets. This value results to be $\sigma_r = 10^7$ km. Similar results can be found in [25], where LoS error statistics as a function of the initial probe position standard deviation are shown. Also in this case, when $\sigma_r \geq 10^7$ km, the image processing algorithm is not able to point the target planet and extract its LoS.

1. Method Selection

The performances of the five alternative filtering schemes described in Sec. III are compared to select the procedure that is most appropriate to be deployed on miniaturized hardware. The drivers that lead the trade-off are 1) the computational time (CPU time) and 2) the maximum value of the conditioning number

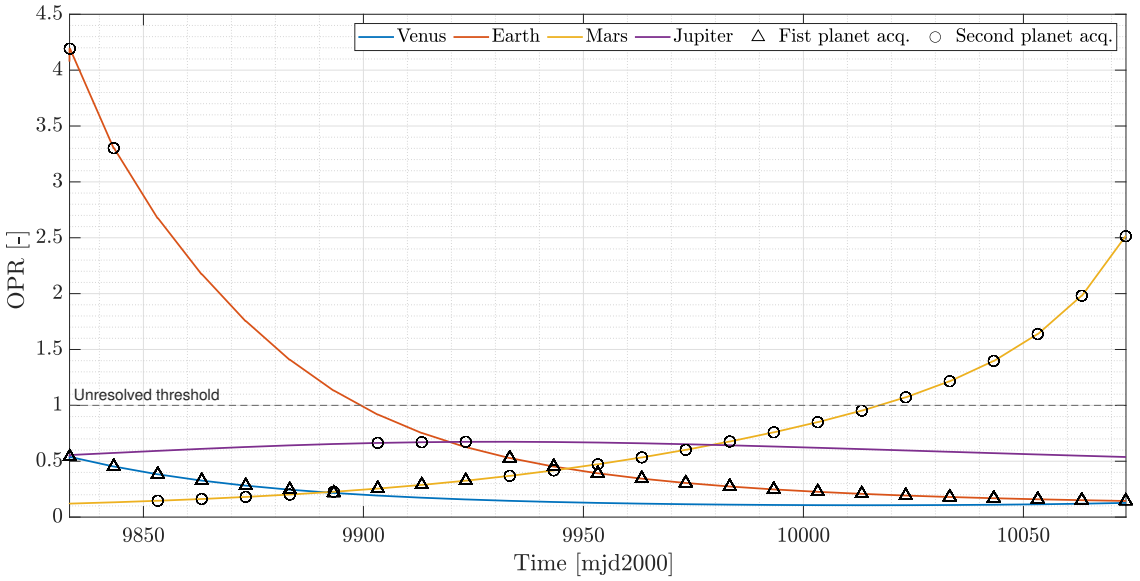

Fig. 12 Planets Object to Pixel Ratio. The triangular and the circular markers highlight the OPR values of the first and second acquired planets, respectively.

of the state error covariance matrix (max $\mathcal{K}$). The former is employed as measure of the computational complexity of the algorithm, whereas the latter indicates the filter numerical stability. The five alternatives have been tested on 100 samples each on an Intel(R) Core(TM) i7-10700 CPU@2.90 GHz; Table 6 reports average values of the simulations. The parameters employed for the non-dimensionalization are $\bar{r} = 1e4$ km and $\bar{t} = 1e2$ s.

Table 6 Comparison of the alternative filtering procedures

Method	Standard	A	B	C	D
CPU time [s]	6.35	6.54	6.92	5.41	5.56
Max $\mathcal{K}$ [-]	10^{33}	10^{16}	10^{32}	10^{25}	10^{12}

To carry out the trade-off, marks from 1 to 5 are employed, where 1 represents the poorest alternative while 5 the best one. The criteria matrix is so developed:

Table 7 Criteria matrix

Method	Standard	A	B	C	D
CPU time	3	2	1	5	4
Max $\mathcal{K}$	1	4	2	3	5
Total Score	4	6	3	8	9

Method D has the highest score, and it is so selected as the most suited filtering scheme to be deployed on a miniaturized computer. Indeed, thanks to the application of the square-root factorization and the non-dimensionalization strategy, Method D is the most stable over the five alternatives, and the second less complex.

It is important to underline that the solution accuracy reached in the estimation of the state is identical in all methods. Indeed, the alternative filtering approaches enhance only the numerical precision of the standard filtering strategy, and do not affect its physical accuracy.

2. Estimation Accuracy

Figure 13 and 14 show the error profile during the estimation of the position and the velocity by adopting Method D fed by the optimal beacon selection strategy. The samples error profile is displayed with blue solid lines, whereas the orange solid lines and the dashed ones define the 3σ covariance bounds of the samples and the filter, respectively . At the end of the operation window, the 3σ error of the probe position and velocity is lower than 360 km and 0.04 m/s. Since both the planets and the spacecraft lie almost on the ecliptic plane, the x and y components represent the in-plane error, whereas z is the out-of-plane one. The area of the in-plane uncertainty region (see Sec. IV.D.1 for a graphical representation) highly depends on the problem geometry. Whereas, the out-of-plane solution accuracy is related to the radius of the cones at the intersection, which is associated to the planet relative distance from the probe with respect to their relative positions.

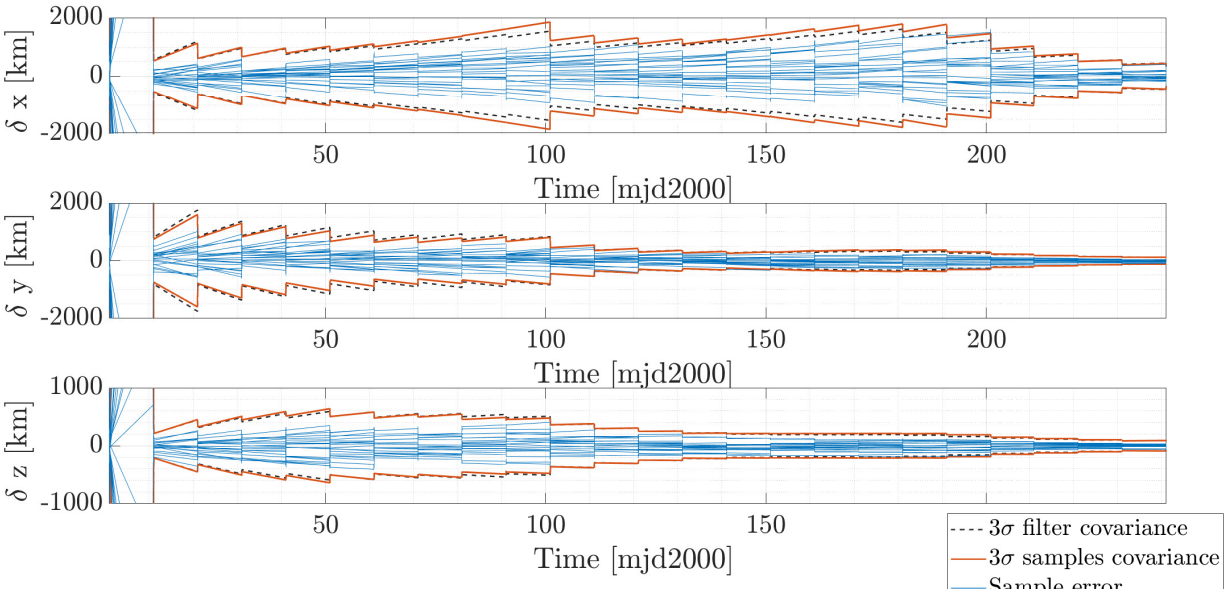

Fig. 13 **Estimated errors for each position component with related 3σ bounds. For clarity sake, only 20 out of 100 Monte Carlo sample histories are reported.**

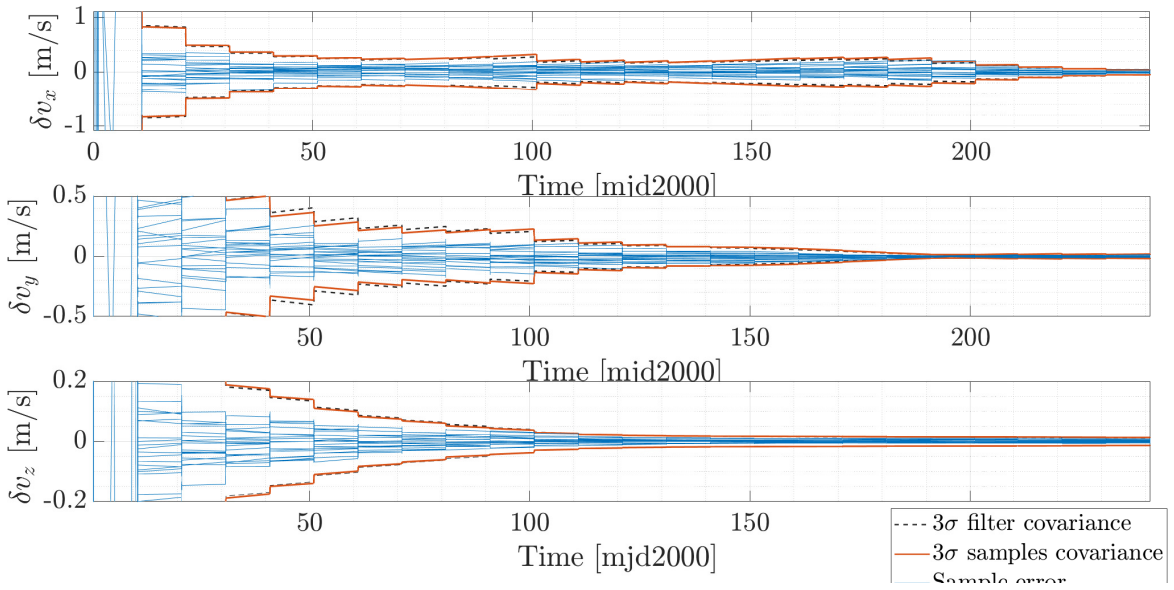

Fig. 14 **Estimated errors for each velocity component with related 3σ bounds. For clarity sake, only 20 out of 100 Monte Carlo sample histories are reported.**

If the beacons are not optimally selected, only one combination of planets, i.e., Mars–Jupiter, can be used for the navigation thanks to the availability of these beacons throughout the operational window. Fig. 15 compares the estimator performances when the optimal planets selection strategy is adopted against the case in which only the couple Mars–Jupiter is tracked. In general, the filter that uses the optimal selection has always the lowest 3σ covariance bound values, so demonstrating the improvement in the estimation.

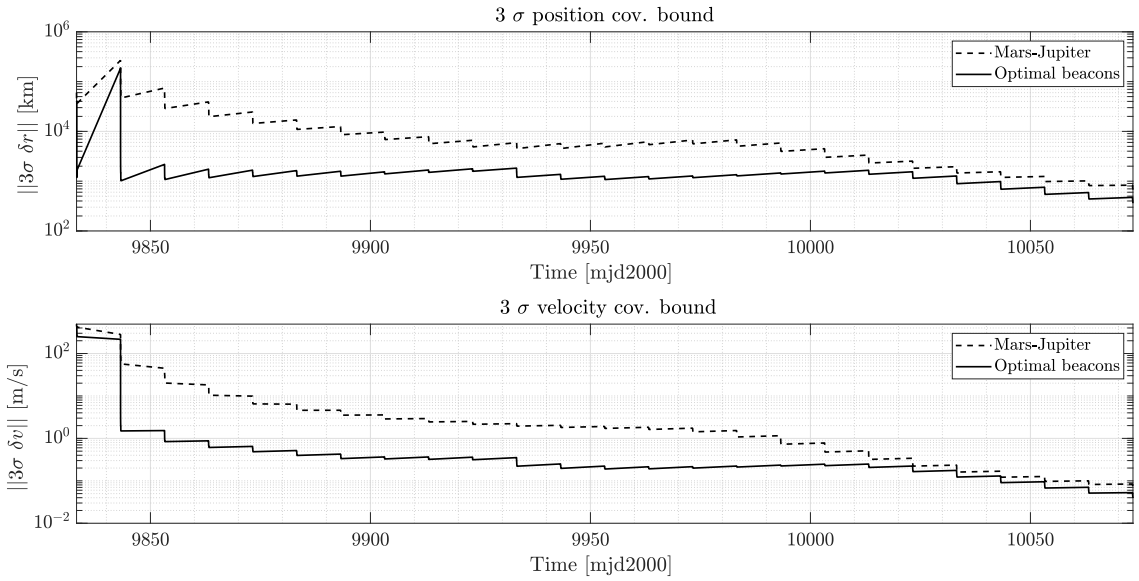

Fig. 15 Comparison between Method D performances obtained when the optimal planets selection strategy is adopted (solid line) and when only the pair Mars–Jupiter is tracked (dashed line).

C. Processor-In-the-Loop Simulation

A Raspberry Pi, whose computational power and size are comparable to a COTS CubeSat on-board computer, is employed to test the estimator performances in a Processor-In-the-Loop (PIL) simulation. The main specifics of the hardware used are given in the Table 8.

Table 8 Raspberry Pi technical specification [‡]

Model	Processor	RAM	OS
Raspberry Pi 4 model B	ARM v8	2GB	Raspberry Pi OS (Linux)

The deployment of Method D on the Raspberry Pi has been performed by exploiting the *Matlab Support Package for Raspberry Pi Hardware* [§] and *Matlab Coder* [¶]. At first, these apps generate automatically an equivalent C++ code starting from a `.m` file by creating a connection between MATLAB and the platform. Then, the coder deploys the algorithm as an executable file on the Raspberry Pi, on which it is run as a standalone application. The inputs of the deployed estimator such as the initial perturbed state and the output vector $\boldsymbol{y}_k$ are simply loaded on the hardware and processed by the filter.

[†] `https://www.raspberrypi.org/products/raspberry-pi-4-model-b/specifications/`, Last Visited on Jan. 2021
[‡] `https://www.raspberrypi.org/products/raspberry-pi-4-model-b/specifications/`, Last Visited on Jan. 2021
[§] `https://it.mathworks.com/help/supportpkg/raspberrypiio/`, Last Visited on January 2021
[¶] `https://it.mathworks.com/products/matlab-coder.html`, Last Visited on January 2021

Fig. 16 Testing of the algorithm performances on a Raspberry-Pi.

The average CPU time required to run the filter over the operational window for 20 simulations is 3.96 s , whereas the solution accuracy reached in the estimation is equivalent to the one in Section IV.B.2 and summarized in Table 9.

Table 9 Solution accuracy at the end of the operational window with PIL simulation

3σ position error [km]	3σ velocity error [m/s]
360	0.039

D. Filter Performances on Different Test Cases

The orbit determination algorithm is tested over two different test cases: A. Toward an outer planet and B. Toward an inner planet. The navigation procedure adopted is the one represented in Fig. 9. The features of the optical sensor and the filter settings are equal to the aforementioned ones if not differently specified.

1. Navigation Toward an Outer Planet

The spacecraft is covering an interplanetary trajectory toward Saturn. At $t_0 = 28.38$ mjd2000, the probe state is described by the Cassini's position and velocity vectors $\tilde{\boldsymbol{r}}_0 = [283.36667.86 - 8.85] \cdot 10^6$ km $\tilde{\boldsymbol{v}}_0 = [-3.11, 11.84, -0.10]$ km/s [‖], respectively. The state of Cassini at t_0 is propagated for 300 days with the dynamic model described in Eq. (15). In this configuration only the planets Saturn-Jupiter are visible, thus they are always selected despite their optimality. The nominal probe trajectory and the result of the optimal planets selection is shown in Fig. 17.

[‖] `https://ssd.jpl.nasa.gov/horizons/`, Last visited on 17th November 2021

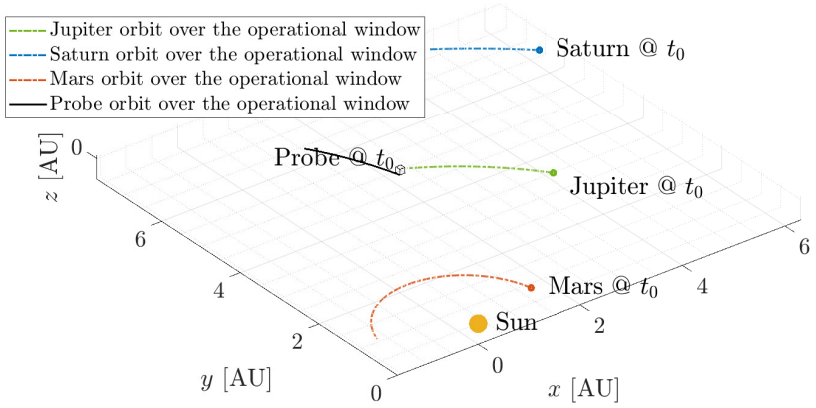

(a) Probe's (solid line) and planets' trajectories (dashed lines) during the operational window.

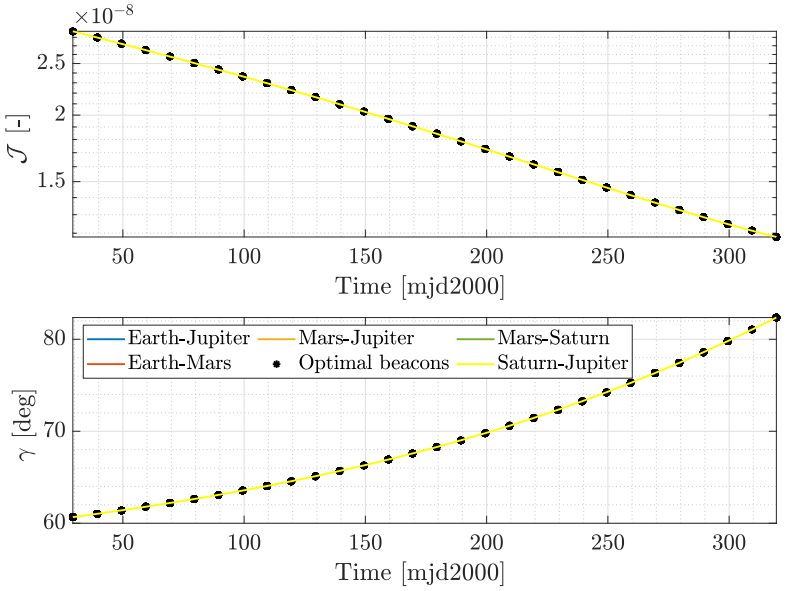

(b) $\mathcal{J}$ and γ trends over the operational window for the only combination of available planets.

Fig. 17 Trajectory and planets selection for Cassini mission

The filter estimates the position and the velocity with a 3σ accuracy of 8226 km and 0.44 m/s, respectively. This worsening of the filter performances mainly happens due to the vast distance between the probe and the observed planets. Let us take as reference Sec. IV.D.1.

The uncertainty region generated by the initial position uncertainty $\boldsymbol{w}$ and measurement error σ is a 3D cone that scales linearly with the relative distance between the probe and the observed object. The intersection region of two uncertainty cones, which represents the state uncertainty, will increase as well, worsening the accuracy of the navigation solution. This is also proved by the $\mathcal{J}$ values in Fig. 17b, which are one order greater in average with respect to the case shown in Fig. 11.

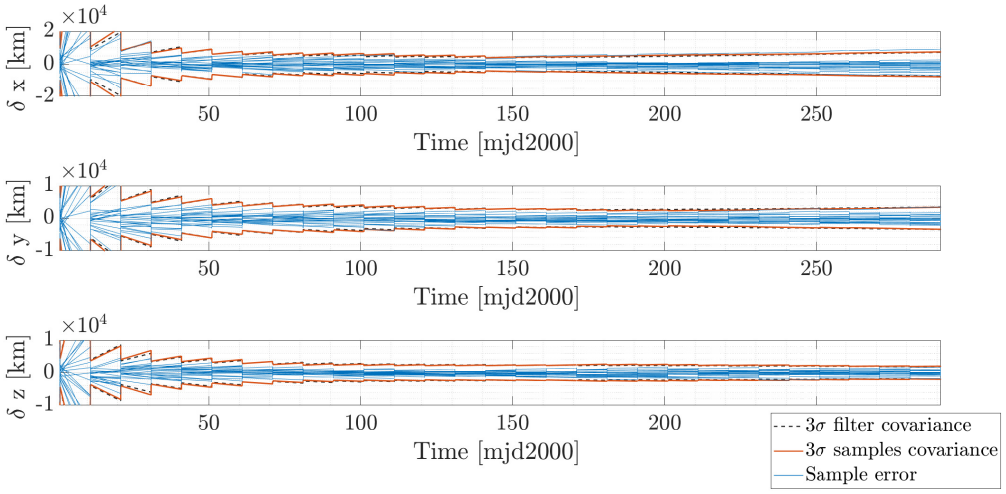

(a) Estimated errors for each position component with related 3σ bounds. For clarity sake, only 20 out of 100 Monte Carlo sample histories are reported.

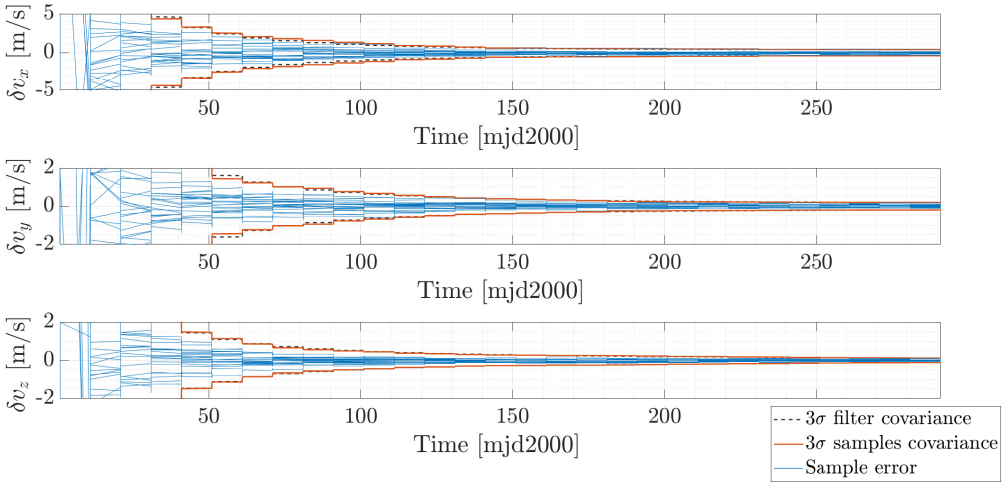

(b) Estimated errors for each velocity component with related 3σ bounds. For clarity sake, only 20 out of 100 Monte Carlo sample histories are reported.

Fig. 18 Filter performances for the Cassini mission

2. Navigation Toward an Inner Planet

The spacecraft is covering an interplanetary transfer toward Venus. At $t_0 = 9121$ mjd2000, the probe state is described by position and velocity vectors $\tilde{\boldsymbol{r}}_0 = [0.024, 1.48, 0.02] \cdot 10^8$ km $\tilde{\boldsymbol{v}}_0 = [-27.49, 0.44, 1.46]$ km/s, respectively. The probe state at t_0 is propagated for 140 days. The nominal probe trajectory and the result of the optimal planets selection is shown in Fig. 19.

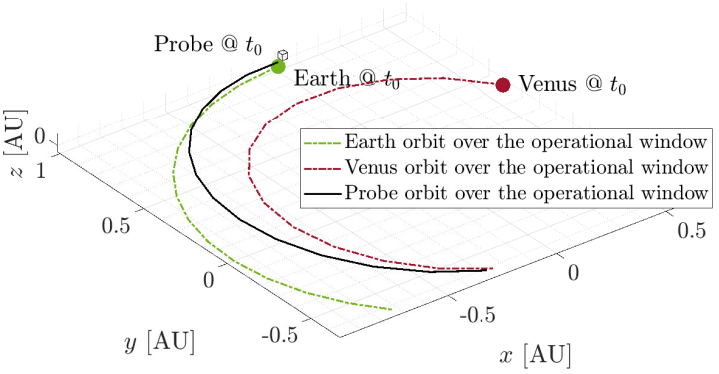

(a) Probe's trajectory (solid line) and departure and arrival planets' trajectories (dashed lines) during the operational window.

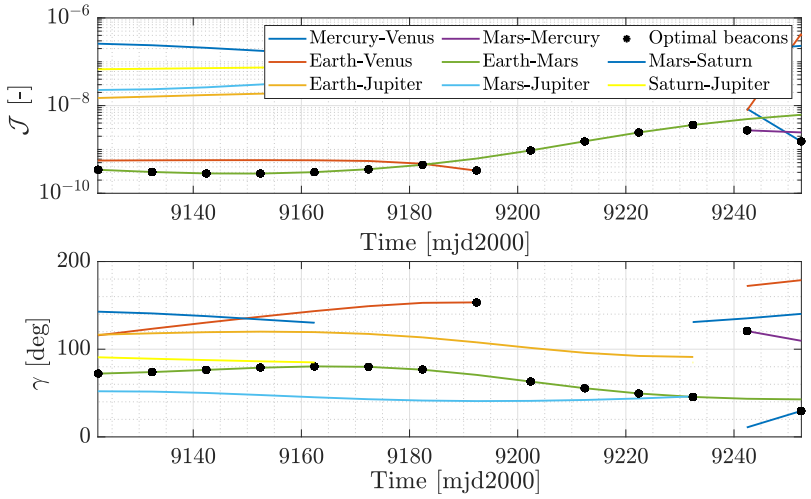

(b) $\mathcal{J}$ and γ trends over the operational window for the combinations of available planets. The optimal selection is represented with black dots.

Fig. 19 Trajectory and planets selection for the Venus transfer

The filter estimates the position and the velocity with a 3σ accuracy of 700 km and 0.2 m/s, respectively. The position and velocity error profiles are shown in Fig. 20. The results obtained are similar to the Earth–Mars transfer's ones. This was expected by noticing that the $\mathcal{J}$ values associated to the selected pair of planets are of the same order of the one obtained for the Earth–Mars transfer.

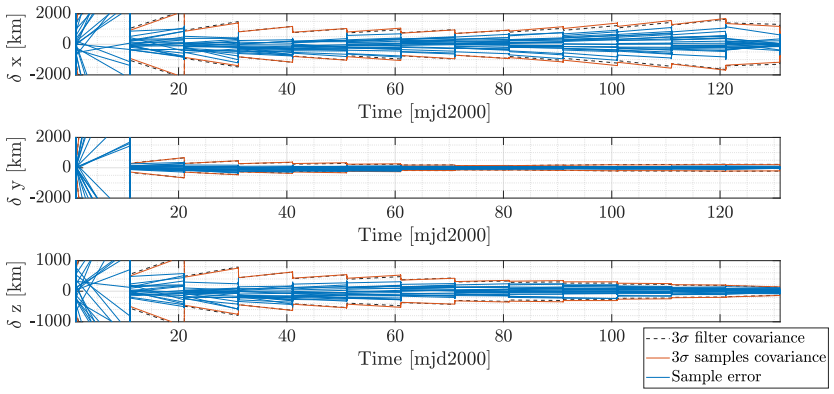

(a) Estimated errors for each position component with related 3σ bounds. For clarity sake, only 20 out of 100 Monte Carlo sample histories are reported.

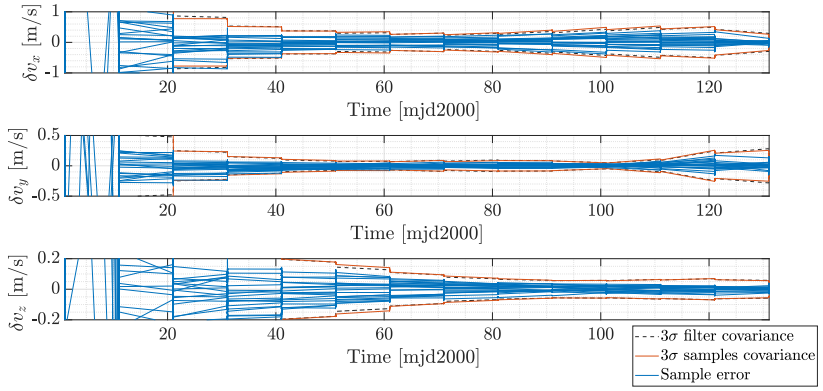

(b) Estimated errors for each velocity component with related 3σ bounds. For clarity sake, only 20 out of 100 Monte Carlo sample histories are reported.

Fig. 20 Filter performances for the Venus transfer

V. Conclusions

This work has investigated the autonomous optical-based OD problem applied to a representative CubeSat processor. An enhancement of the solution accuracy and the estimator numerical stability has been performed thanks to the application of different strategies. The solution accuracy has been improved by selecting the best couples of planets for each navigation leg. Besides, the error resulting from the presence of the light-time effect has been corrected by evaluating the parameter τ after the propagation steps and by retrieving the planet ephemerides at the epoch of light emission. Whereas, the correction of the light aberration effects has been developed every time a new observation is acquired, and before the estimation is measurement-updated. Finally, the EKF performances of different filtering methods have been studied to prevent the rise of numerical issues after the deployment on the hardware. Among the five schemes, the Method D has been selected as the most suited alternative to be exploited for CubeSats application, and it has been deployed on the Raspberry Pi to verify its appropriateness. The filter estimated the probe position and velocity with 3σ bounds of the order

of 360 km and 0.04 m/s, respectively. The suitability of the Method D for CubeSats is so verified.

In this work, the planets LoS direction was only simulated and not extracted from generated sky-field images. Indeed, the next step concerns the development of a robust pipeline for planets LoS extraction and its integration with the presented optical-based orbit determination algorithm. The first results in this direction can be found in [25]. The navigation algorithm will be eventually tested and validated through a hardware-in-the-loop simulation. More details about the navigation experiment that will be carried on within the EXTREMA project are reported in [24].

Acknowledgments

This research is part of EXTREMA, a project that has received funding from the European Research Council (ERC) under the European Union's Horizon 2020 research and innovation programme (Grant Agreement No. 864697).

References

[1] Villela, T., Costa, C., Brandão, A., Bueno, F., and Leonardi, R., "Towards the Thousandth CubeSat: A Statistical Overview," *International Journal of Aerospace Engineering*, Vol. 2019, 2019. https://doi.org/10.1155/2019/5063145.

[2] Poghosyan, A., and Golkar, A., "CubeSat evolution: Analyzing CubeSat capabilities for conducting science missions," *Progress in Aerospace Sciences*, Vol. 88, 2017, pp. 59 – 83. https://doi.org/https://doi.org/10.1016/j.paerosci.2016.11.002.

[3] Walker, R., Binns, D., Bramanti, C., Casasco, M., Concari, P., Izzo, D., Feili, D., Fernandez, P., Fernandez, J., Hager, P., Koschny, D., Pesquita, V., Wallace, N., Carnelli, I., Khan, M., Scoubeau, M., and Taubert, D., "Deep-space CubeSats: Thinking inside the box," *Astronomy & Geophysics*, Vol. 59, 2018, pp. 5.24–5.30. https://doi.org/10.1093/astrogeo/aty232.

[4] Klesh, A., and Krajewski, J., "MarCO: Mars Cube One – Lessons Learned from Readying the First Interplanetary Cubesats for Flight," *49th Lunar and Planetary Science Conference 2018*, 2018.

[5] Hoffman, T., "InSight: Mission to Mars," *2018 IEEE Aerospace Conference*, 2018, pp. 1–11. https://doi.org/10.1109/AERO.2018.8396723.

[6] Speretta, S., Topputo, F., Biggs, J., Lizia, P. D., Massari, M., Mani, K., Tos, D. D., Ceccherini, S., Franzese, V., Cervone, A., Sundaramoorthy, P., Noomen, R., Mestry, S., do Carmo Cipriano, A., Ivanov, A., Labate, D., Tommasi, L., Jochemsen, A., Gailis, J., R.Furfaro, Reddy, V., Vennekens, J., and Walker, R., "LUMIO: achieving autonomous operations for Lunar exploration with a CubeSat," *2018 SpaceOps Conference*, 2018, p. 11. https://doi.org/10.2514/6.2018-2599.

[7] Franzese, V., Di Lizia, P., and Topputo, F., "Autonomous Optical Navigation for the Lunar Meteoroid Impacts Observer," *Journal of Guidance, Control, and Dynamics*, Vol. 42, No. 7, 2019, pp. 1579–1586. https://doi.org/10.2514/1.G003999.

[8] Topputo, F., Wang, Y., C.Giordano, Franzese, V., Goldberg, H., Perez-Lissi, F., and Walker, R., "Envelop of reachable asteroids by M-ARGO CubeSat," *Advances in Space Research*, 2021. https://doi.org/https://doi.org/10.1016/j.asr.2021.02.031.

[9] Goldberg, H. R., Karatekin, O., Ritter, B., Herique, A., Tortora, P., Prioroc, C., Gutierrez, B. G., Martino, P., and Carnelli, I., "The Juventas CubeSat in Support of ESA's Hera Mission to the Asteroid Didymos," *33rd Annual AIAA/USU Conference on Small Satellites*, 2019.

[10] Ferrari, F., Franzese, V., Pugliatti, M., Giordano, C., and Topputo, F., "Preliminary mission profile of Hera's Milani CubeSat," *Advances in Space Research*, 2021. https://doi.org/https://doi.org/10.1016/j.asr.2020.12.034.

[11] Carnelli, I., Martino, P., Escorial, D., Rugina, A., Gil, J., Greus, H., Valverde, A., Zuccaro, A., Bonnafous, B., Moya, C. M., Honvault, C., Lissi, F. P., Tzeremes, G., Khan, M., Küppers, M., Tourloukis, M., Muñoz, P., Concari, P., Moissl, R., and Accomazzo, A., "ESA's Hera mission to asteroid Dimorphos," *Europlanet Science Congress 2020*, 2020. https://doi.org/https://doi.org/10.5194/epsc2020-1119.

[12] Border, J. S., and Thornton, C. L., *Range and Doppler Tracking Observables*, John Wiley & Sons, Ltd, 2000, Chap. 3, pp. 9–46.

[13] Lichten, S. M., Abraham, D. S., Arroyo, B., Asmar, S. W., Bell, J., and Edwards, C. D., "Allocation of Deep Space Network Ground System Tracking and Communications Assets During the 2020-2021 Timeframe of the "Mars Armada"," *2018 SpaceOps Conference*, 2018. https://doi.org/10.2514/6.2018-2502.

[14] Bhaskaran, S., Riedel, J., Synnott, S., and Wang, T., "The Deep Space 1 autonomous navigation system - A post-flight analysis," *Astrodynamics Specialist Conference*, 2000. https://doi.org/10.2514/6.2000-3935.

[15] Bhaskaran, S., "Autonomous Navigation for Deep Space Missions," *SpaceOps 2012 Conference*, 2012. https://doi.org/10.2514/6.2012-1267135.

[16] Vasile, M., Romano, M., and Trainiti, F., "An Optical Based Strategy for Deep Space Autonomous Navigation," *Spacecraft Guidance, Navigation and Control Systems*, ESA Special Publication, Vol. 425, edited by B. Schürmann, 2000, p. 549.

[17] Rufino, G., and Accardo, D., "Enhancement of the centroiding algorithm for star tracker measure refinement," *Acta Astronautica*, Vol. 53, 2003, pp. 135–147. https://doi.org/10.1016/S0094-5765(02)00199-6.

[18] Franzese, V., and Topputo, F., "Optimal Beacons Selection for Deep-Space Optical Navigation," *The Journal of the Astronautical Sciences*, 2020. https://doi.org/https://doi.org/10.1007/s40295-020-00242-z.

[19] Broschart, S. B., Bradley, N., and Bhaskaran, S., "Kinematic Approximation of Position Accuracy Achieved Using Optical Observations of Distant Asteroids," *Journal of Spacecraft and Rockets*, Vol. 56, No. 5, 2019, pp. 1383–1392. https://doi.org/10.2514/1.A34354.

[20] Karimi, R., and Mortari, D., "Interplanetary Autonomous Navigation Using Visible Planets," *Journal of Guidance, Control, and Dynamics*, Vol. 38, 2015, pp. 1–6. https://doi.org/10.2514/1.G000575.

[21] Christian, J. A., "StarNAV: Autonomous Optical Navigation of a Spacecraft by the Relativistic Perturbation of Starlight," *Sensors*, Vol. 19, No. 19, 2019. https://doi.org/10.3390/s19194064.

[22] Franzese, V., Topputo, F., Ankersen, F., and Walker, R., "Deep-Space Optical Navigation for M-ARGO Mission," *The Journal of the Astronautical Sciences*, Vol. 68, No. 3, 2021, pp. 1–20. https://doi.org/10.1007/s40295-021-00286-9.

[23] M. Song, and Y. Yuan, "Autonomous navigation for deep spacecraft based on celestial objects," *2008 2nd International Symposium on Systems and Control in Aerospace and Astronautics*, 2008, pp. 1–4. https://doi.org/10.1109/ISSCAA.2008.4776308.

[24] Di Domenico, G., Andreis, E., Morelli, A. C., Merisio, G., Franzese, V., Giordano, C., Morselli, A., Panicucci, P., Ferrari, F., and Topputo, F., "Toward Self-Driving Interplanetary CubeSats: the ERC-Funded Project EXTREMA," *72nd International Astronautical Congress*, 2021. URL http://hdl.handle.net/11311/1189306.

[25] Bella, S. A., Andreis, E., Franzese, V., Panicucci, P., and Topputo, F., "Line-of-Sight Extraction Algorithm for Deep-Space Autonomous Navigation," *2021 AAS/AIAA Astrodynamics Specialist Conference*, 2021. URL http://hdl.handle.net/11311/1183096.

[26] Mortari, D., and Conway, D., "Single-point position estimation in interplanetary trajectories using star trackers," *Celestial Mechanics and Dynamical Astronomy*, Vol. 128, 2016. https://doi.org/10.1007/s10569-016-9738-4.

[27] Cellino, A., Bagnulo, S., Gil-Hutton, R., Tanga, P., Cañada-Assandri, M., and Tedesco, E. F., "On the calibration of the relation between geometric albedo and polarimetric properties for the asteroids," *Monthly Notices of the Royal Astronomical Society*, Vol. 451, No. 4, 2015, pp. 3473–3488. https://doi.org/10.1093/mnras/stv1188, URL https://doi.org/10.1093/mnras/stv1188.

[28] Mallama, A., and Hilton, J. L., "Computing apparent planetary magnitudes for The Astronomical Almanac," *Astronomy and Computing*, Vol. 25, 2018, pp. 10–24. https://doi.org/10.1016/j.ascom.2018.08.002.

[29] Whitmell, C. T., "Brightness of a planet," *The Observatory*, Vol. 30, 1907, pp. 96–100.

[30] Jean, I., Ng, A., and Misra, A. K., "Impact of solar radiation pressure modeling on orbital dynamics in the vicinity of binary asteroids," *Acta Astronautica*, Vol. 165, 2019, pp. 167–183. https://doi.org/https://doi.org/10.1016/j.actaastro.2019.09.003.

[31] J. R. Carpenter, C. N. D., "Navigation Filter Best Practices," Tech. Rep. 20180003657, NASA, 04 2018.

[32] Simon, D., *Alternate Kalman filter formulations*, John Wiley & Sons, Ltd, 2006, Chap. 6, pp. 149–181. https://doi.org/10.1002/0470045345.ch6.

[33] Buckingham, E., "On Physically Similar Systems; Illustrations of the Use of Dimensional Equations," *Physical Review*, Vol. 4, No. 4, 1914, pp. 345–376. https://doi.org/10.1103/PhysRev.4.345.